



Galactic Gas Flows from Halo to Disk: Tomography and Kinematics at the Milky Way’s Disk–Halo Interface

Hannah V. Bish¹ , Jessica K. Werk^{1,2} , J. Xavier Prochaska² , Kate H. R. Rubin³ , Yong Zheng^{4,5} ,
John M. O’Meara⁶ , and Alis J. Deason⁷

¹Department of Astronomy, University of Washington, Seattle, WA 98195, USA; hvbish@uw.edu

²UCO/Lick Observatory, University of California, Santa Cruz, CA 95064, USA

³Department of Astronomy, San Diego State University, San Diego, CA 92182, USA

⁴Department of Astronomy, University of California, Berkeley, Berkeley, CA 94720, USA

⁵Miller Institute for Basic Research in Science, University of California, Berkeley, Berkeley, CA 94720, USA

⁶W. M. Keck Observatory, 65–1120 Mamalahoa Highway, Kamuela, HI 96743, USA

⁷Institute for Computational Cosmology, Department of Physics, University of Durham, South Road, Durham DH1 3LE, UK

Received 2019 February 20; revised 2019 July 18; accepted 2019 July 20; published 2019 September 4

Abstract

We present a novel absorption-line survey using 54 blue horizontal branch stars in the Milky Way halo as background sources for detecting gas flows at the disk–halo interface. Distance measurements to high-latitude ($b > 60^\circ$) background stars at 3.1–13.4 kpc, combined with unprecedented spatial sampling and spectral resolution, allow us to examine the 3D spatial distribution and kinematics of gas flows near the disk. We detect absorption signatures of extraplanar Ca II and Na I in Keck HIRES spectra and find that their column densities exhibit no trend with distance to the background sources, indicating that these clouds lie within 3.1 kpc of the disk. We calculate covering fractions of $f_{\text{Ca II}} = 63\%$, $f_{\text{Na I}} = 26\%$, and $f_{\text{H I}} = 52\%$, consistent with a picture of the circumgalactic medium (CGM) that includes multiphase clouds containing small clumps of cool gas within hotter, more diffuse gas. Our measurements constrain the scale of any substructure within these cool clouds to < 0.5 kpc. Ca II and Na I absorption features exhibit an intermediate-velocity (IV) component inflowing at velocities of $-75 \text{ km s}^{-1} < v < -25 \text{ km s}^{-1}$ relative to the local standard of rest, consistent with previously studied H I structures in this region. We report the new detection of an inflow velocity gradient $\Delta v_z \sim 6\text{--}9 \text{ km s}^{-1} \text{ kpc}^{-1}$ across the Galactic plane. These findings place constraints on the physical and kinematic properties of CGM gas flows through the disk–halo interface and support a galactic fountain model in which cold gas rains back onto the disk.

Unified Astronomy Thesaurus concepts: [Circumgalactic medium \(1879\)](#); [Galaxy fountains \(596\)](#); [Milky Way Galaxy \(1054\)](#); [Milky Way Galaxy fountains \(1055\)](#); [Galaxy kinematics \(602\)](#); [Galaxy processes \(614\)](#); [Galaxy infal \(1599\)](#)

1. Introduction

Galaxies like the Milky Way grow via complex processes balancing the supply, consumption, and removal of gas in star-forming regions. Observations of the baryons involved in this cycle are consistent with gas moving in a “galactic fountain” (Bregman 1980), in which hot gas is ejected from the disk via supernovae, stellar winds, and/or an active galactic nucleus (AGN), and then cools and rains back down onto the disk to trigger new star formation (Shapiro & Field 1976; Savage & Sembach 1994; Sembach et al. 2003). This continual cycling of baryons between the halo and disk plays a crucial role in regulating the supply of fuel for star formation and consequently has a major influence on galaxy evolution.

The varied and complex dynamic mechanisms that drive Galactic baryon cycling are not fully understood but may be key to answering long-standing questions about how galaxies sustain star formation, why they become quenched, and the baryons and metals that are “missing” from the disks of star-forming galaxies (Tumlinson et al. 2017). The relative contributions of star-formation-driven winds in the disk, a biconical wind from Galactic center (Su et al. 2010), tidal stripping of satellites, and inflowing gas from the intergalactic medium (IGM; Brooks et al. 2009) are still widely debated (Bordoloi et al. 2014b; Fox et al. 2015).

The diffuse halo extending from the roughly defined boundary of a galaxy’s disk out to its virial radius—the circumgalactic

medium (CGM)—is host to the galactic fountain and serves as a massive reservoir of gas ($> 10^{10} M_\odot$ for L^* galaxies; Stocke et al. 2013; Werk et al. 2014; Stern et al. 2016; Prochaska et al. 2017). However, observations of the CGM are challenging because the gas it contains is approximately a million times less dense than the interstellar medium (ISM) and therefore difficult to detect in emission for single L^* Milky Way–like galaxies at all epochs (Stocke et al. 2013; Werk et al. 2014). Early evidence for its existence emerged when Münch & Zirin (1961) identified Na I and Ca II absorption in the spectra of high-latitude Milky Way stars as a signature of extraplanar gas.

Subsequent work identified halo gas absorption in external galaxies using quasars as background sources (Bahcall & Spitzer 1969; Bergeron 1986). More recently, deep H I 21 cm observations of gas at the disk–halo interface of both the Milky Way and other external, edge-on spiral galaxies have found a so-called halo lag (e.g., Putman et al. 2012). The approximate rate of halo gas rotation decreases with z -height, with a typical velocity drop-off of $15\text{--}30 \text{ km s}^{-1} \text{ kpc}^{-1}$ (e.g., Fraternali et al. 2002; Sancisi et al. 2008; Heald et al. 2011). This observed halo lag has been offered as evidence of an infalling gaseous component of the disk–halo interface (Fraternali & Binney 2006).

Gas at the disk–halo interface is of particular interest because of the rich physical information it contains about material that has cycled through the CGM. Constraints on the content,

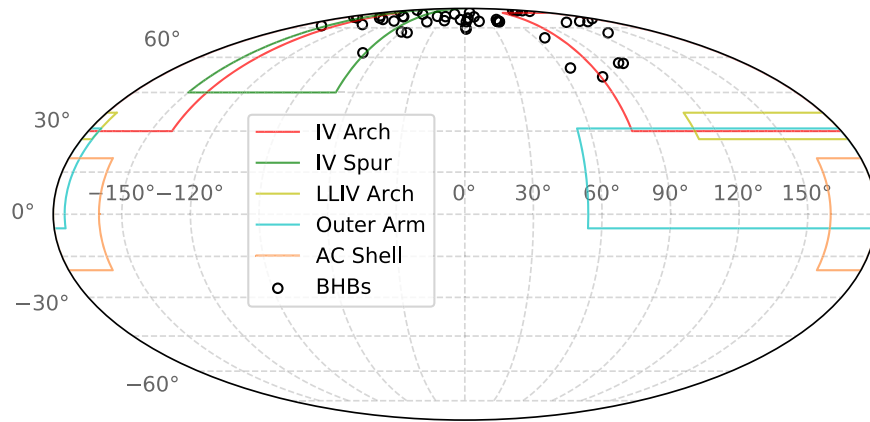


Figure 1. BHB SIGHT LINES AND NEARBY IVCS. Galactic coordinates of the observed BHB sight lines on an all-sky map, along with the approximate boundaries of several large IV H I complexes (van Woerden et al. 2005). The plane of the Milky Way extends horizontally, with Galactic center at $l = 0^\circ$, $b = 0^\circ$. The sight lines probe the boundaries of the high-latitude IVCs known as the IV Arch and the IV Spur.

kinematics, and spatial extent of this material can ultimately point to its origin, but direct detection via emission is possible only for the densest material in the Milky Way halo. Full-sky H I 21 cm emission maps reveal a population of neutral intermediate-velocity clouds (IVCs, $25 \text{ km s}^{-1} < |v| < 90 \text{ km s}^{-1}$ relative to the local standard of rest [LSR]) at heights of $\sim 0.5\text{--}3$ kpc above the disk (Kuntz & Danly 1996; Wakker 2001; Smoker et al. 2011). IVCs are found at predominantly negative velocities (Wakker 2001), and like high-velocity clouds in the halo, their gas is multiphase (Albert & Danly 2004; Lehner & Howk 2011; Fox et al. 2014; Richter 2017). They are thought to contain material that once originated in the Galaxy’s disk because their metallicities are consistent with that of Milky Way ISM gas and because ISM simulations find that IVC morphology and kinematics are reproduced by ISM ejecta (Bregman 1980; de Avillez 2000; Ford et al. 2010; Richter 2017).

The timescales on which this material accretes and the phase structure of the clouds themselves are two of the physical properties that can best constrain models of the galactic fountain. However, isolating halo gas from disk gas at the interface is challenging because line-of-sight observations themselves do not provide distance information about the gas, and the two components may overlap partially in velocity space.

Within the past decade, significant advances have been made with improved spectral analysis techniques and the installation of the Cosmic Origins Spectrograph (COS) on the *Hubble Space Telescope* (HST), which increased the sensitivity of diffuse gas detections by an order of magnitude (Osterman et al. 2009). Today, the technique most sensitive to low-density gas along individual sight lines uses spectra of background sources to identify absorption features from foreground gas. These background sources may be quasars observed through the CGM of foreground galaxies (e.g., Werk et al. 2013; Zheng et al. 2017) or halo stars behind Milky Way CGM gas (e.g., Savage & Wakker 2009; Lehner & Howk 2011; Fox et al. 2015). Additionally, the “down-the-barrel” technique measures a galaxy’s CGM in absorption using its own starlight as a background source and has been used to study outflows and accretion (e.g., Rubin et al. 2012; Heckman et al. 2015).

We present an absorption-line survey designed to examine the kinematics, spatial extent, and cloud characteristics of gas at the Milky Way’s disk–halo interface. We have analyzed Ca II ($\lambda\lambda 3934, 3969$) and Na I ($\lambda\lambda 5891, 5897$) transitions in

absorption along 54 sight lines to blue horizontal branch stars (BHBs) with well-constrained heights 3.1–13.4 kpc above the disk. Because they are approximate standard candles, BHBs provide distances that we can use to describe the 3D spatial extent of the gas. The sight lines are limited to high Galactic latitudes ($b > 60^\circ$) so that radial velocity measurements place the greatest possible constraints on gas inflow/outflow velocities. The excellent resolution of Keck HIRES spectra and the unprecedented 3D spatial sampling of this survey allow us to place empirical constraints on the physical and kinematic properties of CGM gas flows through the disk–halo interface.

This paper is organized as follows: In Section 2 we describe the survey design and observations. In Section 3 we describe our methods for line profile fitting and define subsamples for analysis. In Section 4 we present the column density and velocity measurements of the gas absorbers in this sample. In Section 5 we examine how these measurements can place constraints on cloud size and distribution and the implications of our findings for potential origins of the gas we see. In Section 6 we summarize our findings.

2. Observations

2.1. Survey Design and Sample Selection

Our absorption-line survey uses BHBs in the Milky Way halo as background sources to study diffuse foreground gas. BHBs are well suited for this purpose because they have bright, relatively featureless spectra ideal for absorption-line analysis, and as approximate standard candles they have measured distances to within $\pm 10\%$ (Kinman et al. 1994; Sirko et al. 2004; Clewley & Jarvis 2006; Xue et al. 2008; Deason et al. 2011). We have taken advantage of these properties to obtain kinematic information and distance constraints for gas along sight lines that probe the disk–halo interface of the Milky Way. We observed 56 out of 83 stars meeting the selection criteria described in this section and ultimately excluded two from our analysis. Figure 1 shows the Galactic coordinates of the sight lines on an all-sky map, along with the approximate boundaries of several large intermediate-velocity (IV) H I complexes (van Woerden et al. 2005). A full list of these targets and their properties can be found in Table 1.

The sample of background sources was selected from >4500 BHB stars with accurate distances and velocities in the SDSS SEGUE catalog (Xue et al. 2011). To verify that we are using

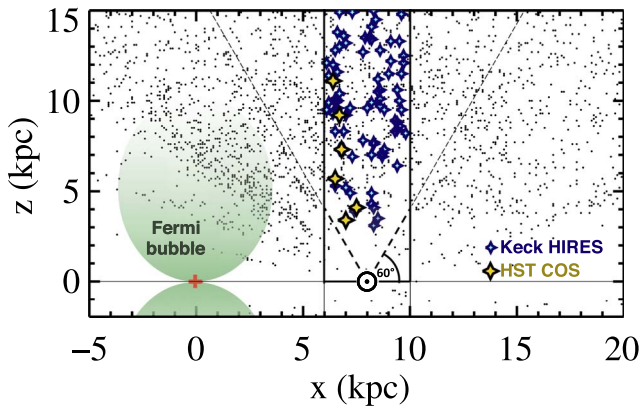


Figure 2. SURVEY GEOMETRY. Spatial distribution of BHB stars in the northern Milky Way halo, shown in the x - z projection. The full BHB catalog from SEGUE (Xue et al. 2011) is displayed with black points. Targets observed with Keck HIRES for this study are highlighted with star symbols and were selected to fall at high Galactic latitudes within a cylinder 2 kpc in radius centered on the Sun. Yellow stars indicate BHBs that have also been observed with *HST* COS as part of a complementary program to study highly ionized gas in this regime. The red plus sign marks the Galactic center, and the Sun is marked by the solar symbol. Green shading indicates the approximate extent of the Fermi bubbles formed by winds emanating from the Galactic center (Su et al. 2010). The three targets at $b > 60^\circ$ are included here but do not appear below the dashed line at $b = 60^\circ$ as viewed from this particular angle.

the best available distance measurements for the BHBs, we checked the SEGUE distances against the *Gaia* DR2 catalog. We found that for all but one BHB, SEGUE distances were more precise because the stars are close to or beyond the ~ 5 kpc limiting distance for accurate parallax measurement (Luri et al. 2018). Since the distance measurements we use only set an upper limit on the distance to the absorbing gas, and most of the gas likely sits close to the disk at small distances (see Section 4.1), the error on BHB distance measurements does not significantly affect our analysis.

Figure 2 shows the distribution of SEGUE BHBs from an edge-on view of the Milky Way. The full set of BHBs in the catalog is marked by small black points, and blue stars show the location of BHBs selected for this study. A subset of these sight lines, shown in yellow, have also been observed with *HST* COS in the UV, and data will be presented in Werk et al. (2019). The Galactic center is indicated with a red plus sign, and the approximate extent of the Fermi Bubbles is shown in green (Su et al. 2010). Fermi Bubbles have been probed in absorption by Bordoloi et al. (2017) using halo stars with known distances, and other work has examined them as a potential source of recycled gas observed elsewhere in the Milky Way (Fox et al. 2015; Karim et al. 2018).

This sample meets several selection criteria. First, targets are bright enough to reach signal-to-noise ratio (S/N) ≥ 10 with Keck/HIRES in less than ~ 1 hr so that absorption features of interest can be detected. This constraint imposes a g -band magnitude cut of $m_g < 16.5$. Figure 3 shows the distribution of g -band magnitudes for background sources in this work and their distances from the Sun. The distance calibrations are dependent on both g magnitude and $(g-r)$ color (Xue et al. 2008). Recently, Lancaster et al. (2018) found that roughly 10% of stars in the SDSS BHB sample were contaminant blue straggler stars, which are fainter than BHBs and would lead to overestimated distances. We have applied their color cut to the BHB catalog to remove these contaminants.

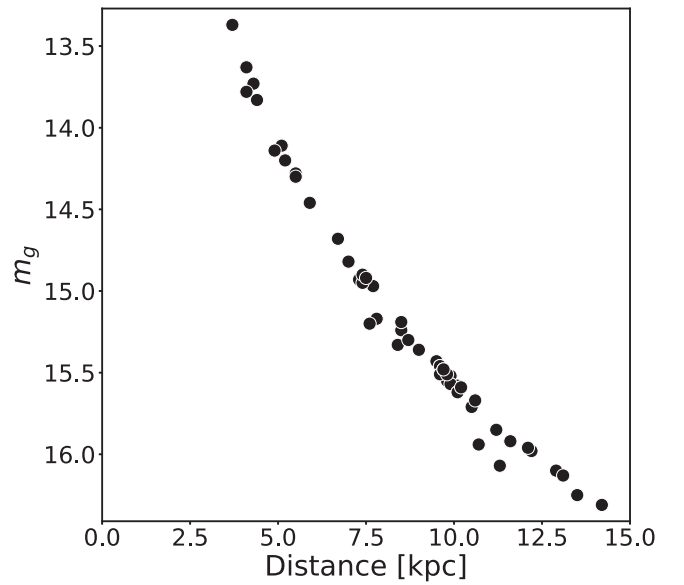


Figure 3. BACKGROUND SOURCE MAGNITUDES. The SDSS apparent g -band magnitude of each background source and its distance from the Sun. The sources are BHB stars, which are approximate standard candles and can be used to constrain the distance to foreground gas along each sight line. Distance calibrations are dependent on both g magnitude and $(g-r)$ color (Xue et al. 2008).

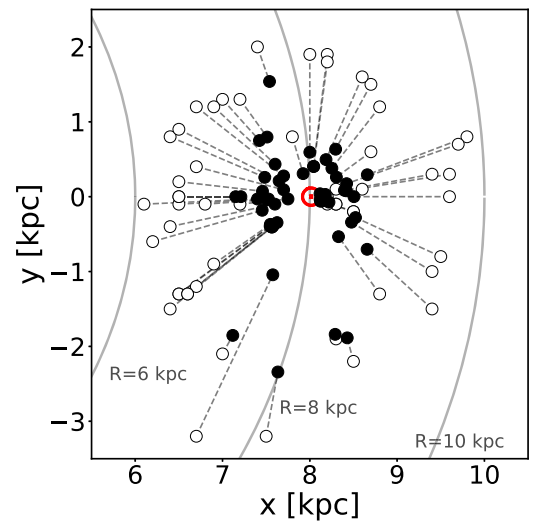


Figure 4. EFFECT OF HEIGHT ASSUMPTIONS ON GAS COORDINATES. An illustration of the change in x - y coordinates for hypothetical gas along each sight line when we assume two different distances to the gas. Open circles mark the coordinates of the upper limit on distance set by the background star. Filled circles, connected by a dashed line, show the location of gas along the same sight line assuming a height of $z = 3$ kpc. The red solar symbol marks the position of the Sun, and lines of constant distance from Galactic center are shown in gray.

Second, we excluded background BHBs with radial velocities $-80 \text{ km s}^{-1} < v_{\text{star}} < 0 \text{ km s}^{-1}$ so that absorption features of the background star and foreground gas would not overlap. This constraint was determined after an initial pilot study showed that virtually all foreground gas fell within that velocity range (see Section 4.2 for discussion of these results).

To place robust constraints on the kinematics of gas inflows/outflows, we selected high-latitude sight lines so that measured radial velocities will best constrain the motion of this gas. High-latitude sight lines provide a window into the dynamics

Table 1
BHB Background Sources

Name	R.A. (h:m:s)	Decl. (°:′:″)	x (kpc)	y (kpc)	z (kpc)	Distance (kpc)	b (deg)	l (deg)	HRV (km s ⁻¹)
J1149+2828	11:49:19.16	+28:28:06.7	9.8	0.8	8.2	8.5	76.2	203.8	102.9
J1204+1947	12:04:05.42	+19:47:43.6	8.7	1.5	7.1	7.3	76.9	244.5	-205.2
J1212+2826	12:12:18.09	+28:26:02.0	9.7	0.7	12.1	12.2	81.3	202.1	40.6
J1215+2315	12:15:59.62	+23:15:57.9	8.8	1.2	9.5	9.6	81.1	236.7	61.9
J1215+3202	12:15:01.55	+32:02:20.1	9.6	0.0	9.5	9.7	80.7	178.9	-88.4
J1216+3308 ^a	12:16:00.06	+33:08:56.2	9.4	-0.2	8.4	8.6	80.3	172.6	39.8
J1216+3004	12:16:53.67	+30:04:08.7	9.6	0.3	11.5	11.6	81.9	189.7	59.2
J1217+2104	12:17:21.04	+21:04:11.1	8.6	1.6	9.7	9.9	80.2	249.0	-129.4
J1218+2951	12:18:00.44	+29:51:38.3	9.4	0.3	10.6	10.7	82.2	190.6	-166.9
J1219+2559	12:19:25.79	+25:59:43.0	8.7	0.6	6.9	7.0	82.8	220.1	174.2
J1223+0002	12:23:55.21	+00:02:20.9	7.4	2.0	3.9	4.4	62.1	288.1	139.8
J1223+3641	12:23:26.85	+36:41:11.1	9.5	-0.8	8.6	8.7	78.8	153.0	-80.4
J1226+1749	12:26:45.86	+17:49:52.0	8.0	1.9	9.6	9.8	79.1	270.2	60.5
J1229+2101	12:29:47.49	+21:01:35.9	8.2	1.9	14.1	14.2	82.2	262.8	211.2
J1230+2052	12:30:22.97	+20:52:21.9	8.2	1.8	13.4	13.5	82.1	264.3	174.2
J1231+3719	12:31:10.44	+37:19:08.4	9.4	-1.0	8.8	9.0	79.0	144.4	-168.0
J1234+4437	12:34:32.86	+44:37:32.1	9.4	-1.5	6.4	6.7	72.2	132.8	48.7
J1236+2837	12:36:51.75	+28:37:36.0	8.6	0.1	10.1	10.1	86.5	187.1	-195.8
J1239+2937	12:39:18.13	+29:37:52.8	8.3	-0.1	4.1	4.1	86.3	169.1	58.8
J1240+2746	12:40:54.84	+27:46:40.6	8.3	0.1	7.7	7.7	87.6	196.8	111.6
J1241+2909	12:41:17.48	+29:09:14.4	8.2	0.0	4.3	4.3	87.0	170.2	-69.9
J1242+2126	12:42:03.34	+21:26:04.2	7.8	0.8	7.8	7.8	83.9	281.9	-71.3
J1243+2842	12:43:50.94	+28:42:35.8	8.3	-0.1	7.6	7.6	87.7	169.2	-102.8
J1243+2931	12:43:39.02	+29:31:49.1	8.2	-0.1	4.9	4.9	87.0	158.0	17.2
J1244+2926	12:44:18.54	+29:26:19.4	8.5	-0.2	11.2	11.2	87.2	156.7	99.5
J1244+2939	12:44:16.47	+29:39:45.3	8.5	-0.2	10.5	10.5	87.0	154.4	-191.6
J1248+0947	12:48:10.28	+09:47:34.4	7.2	1.3	4.9	5.1	72.7	300.2	80.2
J1251+3849	12:51:11.16	+38:49:54.1	8.8	-1.3	7.3	7.4	78.3	123.2	-104.7
J1255+0924	12:55:42.55	+09:24:23.4	7.0	1.3	5.2	5.5	72.3	306.4	150.2
J1257+1741 ^a	12:57:57.64	+17:41:51.1	7.0	1.1	9.2	9.3	80.4	312.3	41.3
J1258+1939	12:58:58.86	+19:39:29.1	6.7	1.2	13.0	13.1	82.3	316.4	-162.3
J1259+1552	12:59:53.71	+15:52:27.7	6.9	1.2	8.3	8.5	78.6	313.3	47.1
J1306+2003	13:06:25.42	+20:03:42.3	6.5	0.9	12.8	12.9	82.1	329.6	27.4
J1307+2224	13:07:00.15	+22:24:25.7	6.7	0.4	13.0	13.1	84.1	340.6	187.9
J1310+2514	13:10:40.39	+25:14:17.4	7.2	-0.1	9.6	9.6	85.2	10.4	38.4
J1314+1751	13:14:13.24	+17:51:57.6	6.4	0.8	9.3	9.5	79.4	333.7	-31.3
J1324+2038	13:24:36.40	+20:38:17.1	6.5	0.2	8.3	8.4	80.0	354.1	28.5
J1324+2418	13:24:53.36	+24:18:36.2	6.4	-0.4	12.0	12.1	82.0	14.3	100.1
J1325+2232a	13:25:26.16	+22:32:20.5	6.5	-0.1	9.5	9.6	81.0	4.0	-148.4
J1325+2232b	13:25:54.40	+22:32:50.1	6.8	-0.1	7.3	7.4	80.9	4.4	-100.3
J1332+2054	13:32:56.98	+20:54:41.5	6.1	-0.1	9.5	9.7	78.7	1.9	109.7
J1335+2820	13:35:47.01	+28:20:41.2	6.7	-1.2	10.4	10.6	80.1	42.6	135.3
J1338+2345	13:38:25.33	+23:45:51.6	6.2	-0.6	9.9	10.1	78.9	17.9	-87.8
J1341+2801	13:41:18.85	+28:01:56.3	6.5	-1.3	9.9	10.1	78.9	40.5	-142.4
J1341+2806	13:41:52.29	+28:06:04.3	6.9	-0.9	7.3	7.5	78.8	40.8	-166.8
J1341+2823	13:41:19.85	+28:23:58.6	6.4	-1.5	11.1	11.3	78.9	42.4	-124.8
J1341+2824	13:41:27.90	+28:24:29.9	6.5	-1.3	10.0	10.2	78.9	42.4	-133.4
J1341+2829	13:41:38.30	+28:29:54.4	6.6	-1.3	10.0	10.2	78.8	42.9	-134.6
J1342+2828	13:42:43.32	+28:28:15.8	6.6	-1.3	9.6	9.8	78.6	42.7	-128.8
J1344+1842	13:44:04.41	+18:42:59.1	6.5	0.0	5.7	5.9	75.3	0.9	-74.7
J1347+1811	13:47:49.70	+18:11:43.6	6.5	0.0	5.3	5.5	74.2	1.4	18.2
J1413+5621	14:13:37.73	+56:21:57.7	8.5	-2.2	3.5	4.1	57.3	101.9	20.2
J1415+3716	14:15:57.13	+37:16:58.1	6.7	-3.2	9.2	9.9	69.5	67.9	-134.0
J1420+5520	14:20:43.45	+55:20:35.0	8.3	-1.9	3.1	3.7	57.5	99.2	-89.3
J1527+4027	15:27:50.05	+40:27:28.9	7.0	-2.1	3.4	4.1	55.2	65.6	-105.6
J1534+5015	15:34:11.23	+50:15:56.3	7.5	-3.2	4.1	5.2	51.4	81.0	-129.4

Note. Properties of BHBs used as background sources to measure gas absorption. The BHB coordinates are given for a Cartesian system in which the x -axis extends from Galactic center in the direction of the Sun, y is perpendicular to x in the plane of the disk, and z is perpendicular to the disk such that the system is right-handed, with positive z toward the north Galactic pole (see Section 2.2). HRV is the heliocentric radial velocity of the BHB, and b and l are Galactic latitude and longitude, respectively. Coordinates and distance measurements were obtained from the SDSS SEGUE catalog (Xue et al. 2011). Errors on distance measurements are approximately 10%.

^a Excluded from sample because of poor data quality.

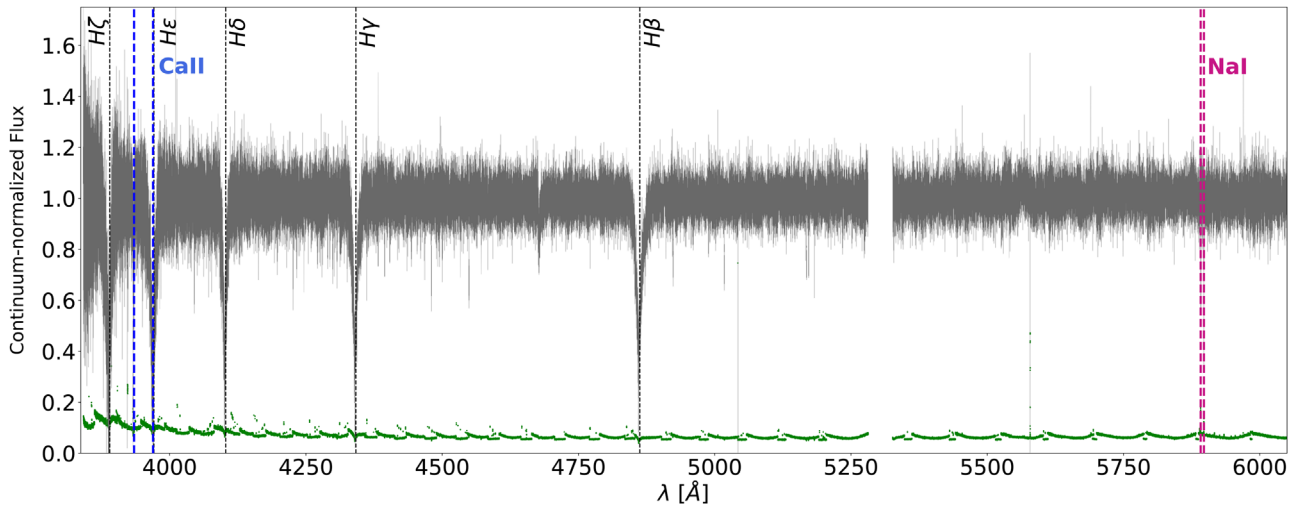


Figure 5. SPECTRUM OF BHB USED AS BACKGROUND SOURCE. Keck HIRES spectrum of J1217+2104, a typical metal-poor BHB used as a background source. Flux measurement error is shown in green. Vertical lines mark stellar Balmer absorption features, as well as the Ca II ($\lambda\lambda 3934.8, 3969.6$) and Na I ($\lambda\lambda 5891.6, 5897.6$) absorption doublets used in this work. Note that the Ca II $\lambda 3969.6$ line falls within the broad H ϵ feature and that the continuum was adjusted to account for this feature before fitting the Ca II doublet. A CCD chip gap falls at 5282–5326 Å. The jagged profile of the flux error is due to the blaze function of each order, which results in more flux at the center of the order than at the edges.

of extraplanar gas flows because we can examine the component of line-of-sight velocities normal to the disk. The target BHB sight lines lie at Galactic latitudes $b > 60^\circ$, with the exception of three from the initial pilot study at $b = 51.4^\circ, 55.2^\circ, \text{ and } 57.5^\circ$.

Finally, we defined a uniform sampling region in projected x - y space across the disk to allow for comparison of extraplanar gas properties at different heights. Since the disk area spanned by BHBs at $b > 60^\circ$ increases with distance, spatially uniform sampling requires that the radius of this cylinder is limited by the number of available sight lines at small heights above the disk. To achieve this uniform sampling, we chose sight lines that lie within a cylinder 2 kpc in radius, centered on the Sun and extending 15 kpc into the halo (Figure 2).

2.2. Coordinate System

BHB distance measurements allow us to adopt 3D coordinates, rather than sky coordinates, to map the distribution of gas. A 3D coordinate system is useful for studying flows in the frame of the Milky Way and is typical for Milky Way dynamical measurements, but it is not often used in absorption studies because distance measurements are rarely available or are too imprecise. Throughout this paper we use a Cartesian coordinate system in our discussion of the position, scale, and kinematics of gas near the disk. The x -axis extends from Galactic center in the direction of the Sun, y is perpendicular to x in the plane of the disk, and z is perpendicular to the disk such that the system is right-handed, with positive z toward the north Galactic pole. In this reference frame, the Galactic center is at the origin and the Sun lies at $(x, y, z) = (8, 0, 0)$ kpc. Figure 2 shows an edge-on view of the Milky Way in the x - z plane, and Figure 4 shows a face-on view of the disk with BHB coordinates projected onto the x - y plane.

We note that the BHB distance measurements represent an upper limit on the distance to any gas detected along the line of sight. Therefore, any distances inferred from spatial maps of gas absorption are upper limits. To illustrate this point, Figure 4 provides a visual comparison of the x - y coordinates of gas

along each sight line assuming two different distances. Coordinates of the upper limit on distance set by the background star are marked by open circles. These are connected by a dashed line to filled circles marking the coordinates of gas along the same line of sight, assuming that all gas lies at a height of $z = 3$ kpc (the motivation for making such an assumption is discussed in Section 4.1). Although the disk area covered by this survey changes significantly, the results we present remain qualitatively the same regardless of the distance assumed. For that reason, we show only the coordinates corresponding to the background source in all subsequent plots unless otherwise noted.

2.3. Keck HIRES Spectra

At optical wavelengths, the HIRES spectrometer (Vogt et al. 1994) at the W. M. Keck Observatory can detect relatively weak absorption features of neutral and low-ionization species like Ca II H+K and Na I D, which trace cool gas ($T \lesssim 10^4$ K) (Spitzer 1956; Münch & Zirin 1961). Figure 5 is an example of a typical BHB spectrum and shows where the Ca II and Na I absorption features fall with respect to the broad stellar Balmer lines. Columns 1 and 2 of Figure 6 show a more detailed view of the Ca II K and Na I D₂ absorption features for selected sight lines. We obtained HIRES spectra for 56 out of 83 total stars that met the criteria outlined above. Two spectra with $S/N < 6$ were ultimately excluded from the sample because S/N was too low for reliable line profile fitting.

Observations were made over two runs in 2016 March and 2017 February, and the instrument setup was chosen to optimize measurement of the Ca II H+K ($\lambda\lambda 3934.8, 3969.6$) and Na I D ($\lambda\lambda 5891.6, 5897.6$) doublets. We took a minimum of two exposures for each sight line to allow for cosmic-ray correction. Exposure times ranged from 300 to 1800 s, depending on the apparent magnitude of the target, resulting in $S/N = 6$ –46 pixel^{-1} with a median of 16.2 at wavelengths near the Ca II doublet and $S/N = 9$ –60 pixel^{-1} with a median of 21.5 for the Na I doublet. Typical wavelength coverage was ~ 3800 –8350 Å, and when possible we adjusted wavelength coverage of each chip so that lines of interest would fall within

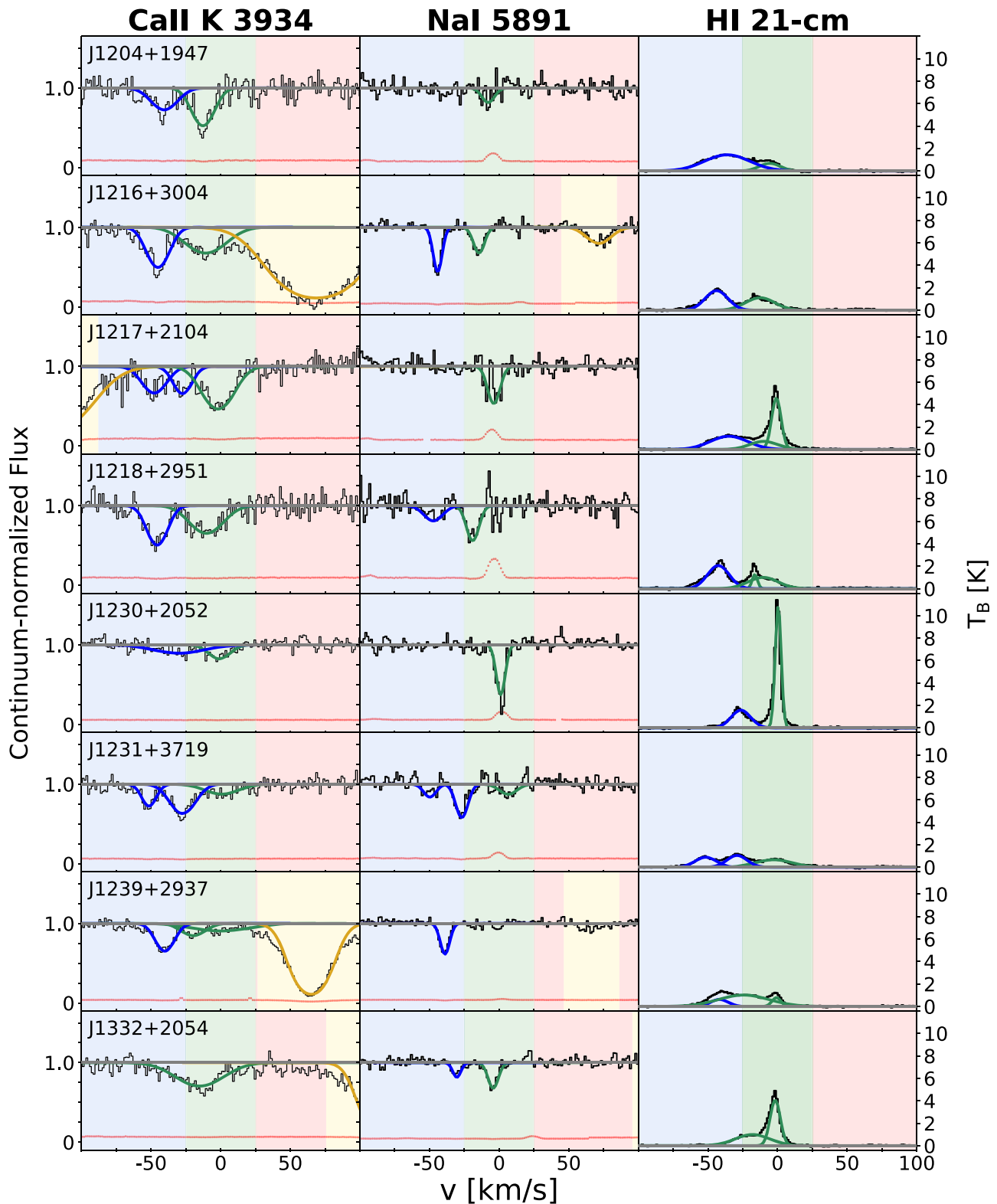


Figure 6. DETAILED VIEW OF ABSORPTION FEATURES. Examples of the Ca II and Na I absorption features marked in Figure 5 for several BHB sight lines (columns 1 and 2), and HI 21 cm brightness temperatures measured nearest those sight lines (column 3) from the Effelsberg-Bonn HI Survey (Winkel et al. 2016). Flux measurement errors for Ca II and Na I are shown in red. The velocity range and absorption features associated with ISM gas ($|v| < 25 \text{ km s}^{-1}$) are shaded green; otherwise, positive velocities are shaded red and negative velocities are shaded blue. Regions near the stellar radial velocity and any associated absorption are highlighted in yellow if they fall within the window of the plot. While the spectra show stellar Ca II absorption in some cases, they rarely show stellar Na I absorption. Almost all absorption detected outside the ISM velocity range is blueshifted, indicating a gaseous component moving toward the disk at approximately -75 to -25 km s^{-1} . The full set of line profile fits is included in Appendix B.

the overlapping wavelength range detected by both chips. We used the C5 decker, with the image rotator in vertical-angle mode. The C5 decker provides spectroscopic resolution of $1.3 \text{ km s}^{-1} \text{ pixel}^{-1}$ and $R = 36,000$, which corresponds to a velocity FWHM of 8.3 km s^{-1} .

Raw data were reduced using the `HIRedux`⁸ pipeline code included in `XIDL`,⁹ a data-reduction software package. We used the pipeline to combine multiple exposures for each sight line, calibrate spectra using flats and ThAr arcs, determine slit profiles for each order, perform sky subtraction, and remove cosmic rays. For a more detailed explanation of this procedure, we refer the reader to O’Meara et al. (2015).

Automated flux calibration of HIRES spectra is difficult and unreliable, so each echelle order was examined by eye for continuum fitting. A Legendre polynomial was fit to each order using the AstroPy-affiliated `linetools` package,¹⁰ an open-source code for analysis of 1D spectra. After automated calibration and co-adding of all orders was complete, the continuum was again examined and adjusted by hand by placing or moving anchor points in absorption-free regions. The Ca II K $\lambda 3934$ line often coincided with broad Balmer features in the stellar spectrum, in which case the continuum was adjusted to fit out these features and ensure that they did not affect column density measurements during analysis.

Finally, we corrected for cosmic rays, hot pixels, and gaps in the data that had not been removed by the `HIRedux` pipeline. Each affected pixel was assigned a new value equal to the mean of the nearest unaffected pixels on each side.

3. Analysis

3.1. Line Profile Fitting

For each sight line, we used Ca II and Na I absorption features, along with HI 21 cm emission measurements from the Effelsberg-Bonn HI Survey (EBHIS), to identify distinct components of gas in velocity space and fit line profiles to them. The features and line profiles discussed in this section are shown in Figure 6 for Ca II K ($\lambda 3934$), Na I D₂ ($\lambda 5891$), and HI 21 cm along several sight lines.

3.1.1. Ca II and Na I Absorption

We fit line profiles to the Ca II H+K ($\lambda\lambda 3934.8, 3969.6$) and Na I D ($\lambda\lambda 5891.6, 5897.6$) doublets in order to measure gas velocity v , column density N , and Doppler b parameter b_D . The Doppler parameter is a measure of line width and reflects line broadening caused by both thermal and nonthermal processes. The wavelength range spanned by each absorption feature and initial guesses for the fit parameters were determined by hand using the `PyIGM IGMGUESSES` GUI.¹¹ Individual inspection allowed us to use priors of narrow velocity width and mask regions of severe blending when fitting multiple velocity components, which was crucial for obtaining good fits since all absorption features were fit independently of one another. These initial guesses were then passed to a fitting routine that uses the Markov chain Monte Carlo (MCMC) technique as implemented in the Python package `emcee` (Foreman-Mackey et al. 2013) to calculate posterior probability distribution

functions (PDFs) for each model parameter. We assume that the logarithm of the likelihood function is equal to the distribution of $\chi^2/2$, adopting uniform priors over the parameter ranges $0.5 < b_D < 75$ and $8 < \log N < 13$. We use Markov chains produced by 50 walkers taking 500 steps, with a burn-in of 150 steps. We report the median and ± 34 th percentiles of the marginalized posterior PDFs as the parameter values and uncertainty intervals for each parameter, respectively.

Once the heliocentric velocities were determined by the MCMC fitting routine, they were corrected for motion relative to the LSR along each sight line, so that gas that is moving at the LSR has $v_{\text{LSR}} = 0 \text{ km s}^{-1}$. All velocities in the following discussion are defined relative to the LSR in this way unless otherwise noted. We do not assume rotation for extraplanar gas, as any effects from rotation or halo lag are orthogonal to the inflow velocities we observe. Because our sight lines are at high Galactic latitudes ($b > 60^\circ$, except three at $b = 51^\circ.4, 55^\circ.2, \text{ and } 57^\circ.5$), Galactic rotation effects are not significant for line-of-sight velocities in this sample (Wakker & van Woerden 1991). For the 48/54 sight lines at $b > 70^\circ$, Galactic rotation introduces $< 5\%$ error in velocity, and for the remaining six sight lines at $50^\circ < b < 70^\circ$ the velocity error is $< 12\%$. The inflow velocities we measure vary by considerably more than 12%, which means that the trends we observe are not due to rotation effects. Lastly, if no absorption was detected, noise in the spectra near the wavelength of the line was used to calculate 2σ upper limits on equivalent width and column density. Across all sight lines, the column density detection limit had a median $\log N$ of 10.97 cm^{-2} for Ca II and 10.58 cm^{-2} for Na I.

3.1.2. HI 21 cm Emission

For purposes of comparison to the more complete observations that have been made in HI 21 cm emission, we obtained data from the Effelsberg-Bonn EBHIS HI survey (Winkel et al. 2016) and analyzed HI emission for positions closest to each BHB sight line. The positions do not precisely match our BHB sight lines because of differing spatial resolutions; the effective beam size for EBHIS is $10\prime.8$ compared to the $1\prime.0$ slit used for HIRES observations (Vogt et al. 1994). The spectral resolution of EBHIS is $\sim 1 \text{ km s}^{-1}$. HI brightness temperature profiles were inspected by eye to obtain initial guesses for line profile parameters and determine the number of distinct emission features in velocity space. These components were fit simultaneously to a Gaussian mixture model, which determined the best fit with the Levenberg-Marquardt damped least-squares algorithm using the `SciPy curve_fit` optimizer (Millman & Aivazis 2011). Note that since HI is detected in emission rather than in absorption along BHB sight lines, the upper limits on distance provided by background sources for Ca II and Na I do not apply to HI.

3.2. Isolating Absorption Signatures of the Galactic Fountain

The distances to BHBs set upper limits on the distance to any intervening gas clouds along the line of sight. Because absorption could originate from gas anywhere along the sight line, extraplanar flows cannot be distinguished from the Milky Way ISM concentrated in the Galactic disk using only the upper limits on distance available to us. However, extraplanar gas flows do exhibit kinematic signatures that allow us to differentiate them from Milky Way ISM gas.

⁸ <http://www.uchicago.edu/~xavier/HIRedux/>

⁹ <http://www.uchicago.edu/~xavier/XIDL/index.html>

¹⁰ <https://github.com/linetools/linetools>

¹¹ <https://github.com/pyigm/pyigm>

Table 2
MCMC Best-fit Absorption-line Properties

Name	v_{LSR} (km s $^{-1}$)	Ca II log N	b (km s $^{-1}$)	v_{LSR} (km s $^{-1}$)	Na I log N	b (km s $^{-1}$)
J1149+2828a	$-47.5^{+0.6}_{-0.6}$ $-20.9^{+0.4}_{-0.4}$	$12.22^{+0.03}_{-0.03}$ $12.07^{+0.45}_{-0.23}$	$9.5^{+1.1}_{-1.1}$ $1.2^{+1.4}_{-0.4}$	$-49.0^{+3.5}_{-2.7}$ $-19.7^{+0.7}_{-0.6}$	$11.38^{+0.20}_{-0.13}$ $11.30^{+0.08}_{-0.08}$	$13.5^{+14.9}_{-4.1}$ $2.0^{+1.5}_{-1.1}$ F
J1204+1947a	$-40.6^{+1.5}_{-1.1}$ $-12.7^{+0.6}_{-0.6}$	$12.03^{+0.07}_{-0.06}$ $12.25^{+0.03}_{-0.03}$	$12.2^{+3.9}_{-2.6}$ $9.9^{+1.1}_{-1.1}$	$-8.1^{+1.5}_{-2.4}$...	$11.38^{+0.13}_{-0.19}$...	$4.7^{+3.7}_{-2.5}$...
J1212+2826a	$-47.6^{+2.0}_{-1.8}$ $-19.6^{+0.5}_{-0.5}$	$12.40^{+0.05}_{-0.05}$ $11.83^{+0.04}_{-0.04}$	$19.9^{+2.9}_{-2.3}$ $5.3^{+1.0}_{-1.0}$
J1215+2315a	$-43.1^{+1.5}_{-1.3}$ $-20.1^{+0.5}_{-0.6}$	$12.18^{+0.06}_{-0.05}$ $12.15^{+0.04}_{-0.03}$	$16.5^{+3.6}_{-2.4}$ $8.0^{+1.0}_{-0.9}$	$-47.2^{+3.8}_{-2.4}$ $-20.8^{+0.1}_{-0.1}$	$11.40^{+0.30}_{-0.13}$ $12.23^{+0.06}_{-0.04}$	$14.3^{+22.7}_{-4.7}$ $2.7^{+0.3}_{-0.3}$
J1215+3202a	$-47.8^{+0.7}_{-0.8}$ $-16.9^{+1.1}_{-1.0}$	$12.19^{+0.03}_{-0.03}$ $12.02^{+0.06}_{-0.05}$	$11.3^{+1.6}_{-1.2}$ $10.9^{+2.5}_{-1.8}$	$-16.0^{+0.4}_{-0.3}$...	$11.33^{+0.06}_{-0.05}$...	$1.6^{+0.7}_{-0.5}$...
J1216+3004a	$-44.7^{+0.4}_{-0.4}$ $-10.4^{+1.5}_{-1.0}$	$12.29^{+0.02}_{-0.02}$ $12.30^{+0.06}_{-0.05}$	$9.8^{+0.8}_{-0.8}$ $18.6^{+3.5}_{-2.4}$	$-43.6^{+0.2}_{-0.1}$ $-14.0^{+0.2}_{-0.2}$	$12.03^{+0.06}_{-0.07}$ $11.60^{+0.02}_{-0.02}$	$1.9^{+0.4}_{-0.2}$ $3.8^{+0.5}_{-0.5}$
J1217+2104a	$-44.9^{+1.0}_{-1.1}$ $-24.3^{+1.0}_{-1.0}$	$12.09^{+0.07}_{-0.06}$ $11.97^{+0.10}_{-0.07}$	$10.6^{+3.0}_{-1.6}$ $7.0^{+3.9}_{-1.5}$	$-0.8^{+0.5}_{-0.5}$...	$11.85^{+0.07}_{-0.07}$...	$4.2^{+0.8}_{-0.8}$...
J1218+2951a	$-44.4^{+0.5}_{-0.5}$ $-6.6^{+3.9}_{-3.8}$	$12.24^{+0.03}_{-0.04}$ $12.39^{+0.28}_{-0.24}$	$8.7^{+0.8}_{-0.7}$ $23.5^{+23.2}_{-11.1}$	$-46.0^{+1.3}_{-1.5}$ $-17.8^{+0.4}_{-0.5}$	$11.53^{+0.07}_{-0.07}$ $11.81^{+0.04}_{-0.04}$	$8.0^{+2.5}_{-1.1}$ $4.5^{+1.1}_{-1.0}$
J1219+2559a	$-39.4^{+0.3}_{-0.3}$ $-14.1^{+1.3}_{-2.1}$	$12.43^{+0.02}_{-0.02}$ $12.15^{+0.10}_{-0.07}$	$9.7^{+0.5}_{-0.5}$ $17.6^{+6.7}_{-3.5}$	$-44.0^{+1.2}_{-0.9}$ $-34.0^{+0.9}_{-1.0}$	$11.74^{+0.06}_{-0.06}$ $11.72^{+0.11}_{-0.06}$	$9.1^{+2.4}_{-1.5}$ $7.8^{+3.9}_{-1.7}$
J1223+0002a	$-5.3^{+1.0}_{-1.1}$	$11.63^{+0.05}_{-0.07}$	$7.8^{+2.2}_{-1.7}$
J1223+3641a	$-15.1^{+1.5}_{-1.6}$ $26.1^{+4.3}_{-2.3}$	$12.12^{+0.05}_{-0.05}$ $12.10^{+0.19}_{-0.10}$	$21.3^{+4.2}_{-2.6}$ $23.4^{+15.5}_{-6.3}$	$-7.0^{+0.2}_{-0.2}$...	$11.85^{+0.15}_{-0.09}$...	$1.3^{+0.3}_{-0.3}$...
J1226+1749a	$-52.7^{+1.0}_{-1.7}$ $-16.4^{+1.7}_{-3.6}$ $16.8^{+0.8}_{-0.8}$	$12.07^{+0.11}_{-0.07}$ $11.97^{+0.19}_{-0.11}$ $11.63^{+0.09}_{-0.07}$	$8.3^{+3.1}_{-2.1}$ $12.7^{+9.1}_{-4.3}$ $3.5^{+2.1}_{-1.7}$	$-50.6^{+0.7}_{-0.7}$ $-26.5^{+0.3}_{-0.3}$...	$11.19^{+0.13}_{-0.09}$ $11.52^{+0.09}_{-0.04}$...	$1.7^{+3.9}_{-1.1}$ $2.1^{+1.2}_{-0.9}$...
J1229+2101a	$-22.7^{+8.7}_{-7.1}$	$12.22^{+0.15}_{-0.16}$	$41.9^{+19.2}_{-14.7}$	$-1.3^{+0.9}_{-0.9}$	$11.72^{+0.06}_{-0.08}$	$8.6^{+1.6}_{-1.4}$
J1230+2052a	$-31.8^{+3.8}_{-5.6}$ $-2.8^{+1.0}_{-0.9}$	$11.86^{+0.25}_{-0.12}$ $11.70^{+0.07}_{-0.06}$	$24.5^{+26.7}_{-8.1}$ $8.8^{+2.5}_{-1.7}$	$1.1^{+0.3}_{-0.3}$...	$11.77^{+0.07}_{-0.05}$...	$5.9^{+1.3}_{-1.1}$...
J1231+3719a	$-51.0^{+0.6}_{-0.7}$ $-27.0^{+0.6}_{-0.7}$ $1.6^{+2.3}_{-3.6}$	$11.78^{+0.04}_{-0.05}$ $12.17^{+0.03}_{-0.03}$ $11.66^{+0.21}_{-0.12}$	$5.7^{+5.5}_{-1.4}$ $11.7^{+1.2}_{-1.1}$ $11.3^{+9.7}_{-3.9}$	$-49.4^{+1.0}_{-0.9}$ $-26.4^{+0.3}_{-0.3}$ $6.9^{+1.9}_{-2.7}$	$11.29^{+0.09}_{-0.08}$ $11.77^{+0.03}_{-0.03}$ $11.32^{+0.14}_{-0.14}$	$4.7^{+1.6}_{-1.5}$ $4.3^{+0.7}_{-0.7}$ $7.4^{+4.6}_{-3.0}$
J1234+4437a	$-35.5^{+1.7}_{-1.8}$ $-9.9^{+0.6}_{-0.6}$ $8.5^{+0.5}_{-0.5}$	$12.54^{+0.12}_{-0.06}$ $12.16^{+0.03}_{-0.04}$ $12.15^{+0.04}_{-0.03}$	$26.5^{+10.1}_{-4.8}$ $9.2^{+1.3}_{-1.0}$ $8.4^{+1.4}_{-1.1}$	$-46.0^{+0.7}_{-0.7}$...	$11.42^{+0.05}_{-0.05}$...	$8.2^{+1.7}_{-1.6}$...
J1236+2837a	$-36.5^{+0.7}_{-0.8}$ $-15.5^{+0.7}_{-0.6}$ $-2.6^{+1.9}_{-3.9}$	$11.80^{+0.06}_{-0.05}$ $11.86^{+0.05}_{-0.05}$ $12.00^{+0.19}_{-0.12}$	$8.1^{+1.5}_{-1.2}$ $6.7^{+1.7}_{-1.1}$ $16.1^{+9.1}_{-5.0}$	$-18.2^{+0.5}_{-0.4}$...	$11.48^{+0.04}_{-0.04}$...	$3.2^{+1.2}_{-1.1}$...
J1239+2937a	$-40.5^{+0.3}_{-0.3}$ $-20.0^{+1.0}_{-1.5}$ $-0.5^{+1.7}_{-2.8}$	$12.01^{+0.02}_{-0.02}$ $11.71^{+0.12}_{-0.07}$ $11.68^{+0.31}_{-0.12}$	$8.3^{+0.6}_{-0.5}$ $10.8^{+5.9}_{-2.4}$ $15.5^{+20.8}_{-5.3}$	$-39.2^{+0.2}_{-0.2}$...	$11.67^{+0.03}_{-0.03}$...	$2.3^{+0.4}_{-0.4}$...
J1240+2746a	$-22.2^{+1.3}_{-1.1}$	$12.26^{+0.04}_{-0.04}$	$24.0^{+4.2}_{-3.0}$	$-28.6^{+2.2}_{-2.3}$	$11.49^{+0.06}_{-0.06}$	$16.9^{+3.6}_{-2.7}$
J1241+2909a	$-38.8^{+1.0}_{-1.5}$ $-8.6^{+1.4}_{-2.4}$	$12.21^{+0.06}_{-0.05}$ $11.75^{+0.14}_{-0.10}$	$14.4^{+3.0}_{-2.0}$ $10.4^{+4.9}_{-2.7}$
J1242+2126a	$-30.5^{+0.4}_{-0.5}$ $-11.1^{+2.1}_{-2.8}$	$11.86^{+0.03}_{-0.03}$ $12.01^{+0.15}_{-0.09}$	$5.5^{+0.9}_{-0.7}$ $19.2^{+10.5}_{-4.6}$	$-0.8^{+0.3}_{-0.3}$...	$12.12^{+0.19}_{-0.07}$...	$2.3^{+0.6}_{-0.6}$...
J1243+2842a	$-29.6^{+4.0}_{-3.7}$ $-13.5^{+1.3}_{-1.1}$	$11.76^{+0.17}_{-0.13}$ $12.02^{+0.06}_{-0.06}$	$17.9^{+10.6}_{-5.5}$ $17.0^{+4.2}_{-2.6}$	$-1.9^{+1.2}_{-1.4}$...	$11.59^{+0.07}_{-0.07}$...	$10.3^{+4.2}_{-1.9}$...
J1243+2931a	$-39.6^{+1.0}_{-0.9}$ $-9.5^{+1.7}_{-1.1}$	$11.72^{+0.05}_{-0.05}$ $11.98^{+0.20}_{-0.08}$	$9.1^{+2.1}_{-1.5}$ $11.5^{+9.2}_{-2.6}$	$-21.5^{+2.2}_{-1.2}$ $-8.5^{+0.2}_{-0.2}$	$11.15^{+0.14}_{-0.08}$ $11.55^{+0.02}_{-0.02}$	$7.0^{+4.6}_{-2.2}$ $3.8^{+0.5}_{-0.5}$
J1244+2926a	$-24.0^{+1.9}_{-2.4}$ $-8.9^{+0.7}_{-0.9}$ $19.9^{+1.0}_{-0.9}$	$12.17^{+0.22}_{-0.17}$ $12.27^{+0.03}_{-0.03}$ $11.95^{+0.06}_{-0.06}$	$12.3^{+10.1}_{-4.9}$ $11.4^{+1.5}_{-1.2}$ $9.4^{+2.2}_{-1.6}$	$-24.2^{+0.4}_{-0.4}$ $-6.6^{+0.6}_{-0.7}$...	$11.50^{+0.18}_{-0.15}$ $11.45^{+0.04}_{-0.04}$...	$0.7^{+0.5}_{-0.1}$ $7.3^{+1.3}_{-1.1}$...
J1244+2939a	$-8.4^{+0.5}_{-0.6}$	$12.50^{+0.01}_{-0.01}$	$17.4^{+0.8}_{-0.7}$	$-6.2^{+0.2}_{-0.2}$	$12.16^{+0.01}_{-0.02}$	$5.5^{+0.4}_{-0.4}$
J1248+0947a	$-8.9^{+1.3}_{-0.5}$	$11.87^{+0.12}_{-0.07}$	$11.7^{+5.6}_{-2.5}$	$-10.0^{+0.6}_{-0.3}$	$11.61^{+0.06}_{-0.07}$	$7.9^{+2.3}_{-2.4}$
J1251+3849a	$-51.1^{+5.8}_{-5.5}$	$12.28^{+0.17}_{-0.18}$	$35.8^{+19.3}_{-12.7}$

Table 2
(Continued)

Name	v_{LSR} (km s $^{-1}$)	Ca II log N	b (km s $^{-1}$)	v_{LSR} (km s $^{-1}$)	Na I log N	b (km s $^{-1}$)
	$-29.4^{+0.8}_{-0.8}$	$12.19^{+0.03}_{-0.03}$	$14.8^{+1.7}_{-1.3}$
	$-6.2^{+0.6}_{-0.5}$	$11.93^{+0.04}_{-0.04}$	$7.5^{+1.1}_{-0.9}$
J1255+0924a	$-19.4^{+2.0}_{-1.1}$	$11.92^{+0.15}_{-0.10}$	$13.6^{+7.8}_{-3.2}$	$-15.4^{+4.7}_{-3.3}$	$12.02^{+0.23}_{-0.21}$	$31.4^{+23.6}_{-13.4}$
	$-6.2^{+0.5}_{-0.5}$	$11.75^{+0.04}_{-0.04}$	$6.4^{+1.4}_{-1.2}$	$-6.4^{+0.4}_{-0.4}$	$11.41^{+0.04}_{-0.04}$	$2.8^{+1.3}_{-1.1}$
J1258+1939a	$-13.7^{+4.3}_{-2.6}$	$12.22^{+0.10}_{-0.07}$	$26.0^{+8.0}_{-4.2}$	$0.0^{+0.6}_{-0.5}$	$11.44^{+0.07}_{-0.07}$	$2.7^{+1.5}_{-1.2}$
	$0.9^{+0.9}_{-1.1}$	$11.92^{+0.07}_{-0.05}$	$9.8^{+2.9}_{-1.9}$
	$40.8^{+0.9}_{-0.9}$	$11.55^{+0.06}_{-0.07}$	$5.5^{+1.6}_{-1.5}$
J1259+1552a	$-19.0^{+1.0}_{-0.9}$	$12.24^{+0.10}_{-0.08}$	$6.7^{+3.1}_{-2.4}$
	$-1.4^{+8.0}_{-5.9}$	$12.37^{+0.24}_{-0.23}$	$30.6^{+28.8}_{-14.3}$
J1306+2003a	$-13.7^{+3.1}_{-1.6}$	$12.17^{+0.19}_{-0.08}$	$13.5^{+9.1}_{-3.7}$	$7.8^{+0.2}_{-0.2}$	$11.97^{+0.22}_{-0.15}$	$1.4^{+1.1}_{-0.3}$
	$1.9^{+0.6}_{-0.8}$	$12.34^{+0.05}_{-0.04}$	$10.5^{+1.9}_{-1.5}$
J1307+2224a	$0.8^{+1.9}_{-3.6}$	$11.67^{+0.44}_{-0.23}$	$13.8^{+27.0}_{-7.6}$
J1310+2514a	$-33.8^{+0.9}_{-0.9}$	$11.82^{+0.07}_{-0.07}$	$6.3^{+1.8}_{-1.4}$
	$-9.8^{+3.3}_{-5.7}$	$12.15^{+0.23}_{-0.12}$	$20.9^{+18.7}_{-6.6}$
J1314+1751a	$-2.2^{+0.3}_{-0.3}$	$11.77^{+0.03}_{-0.02}$	$3.7^{+0.7}_{-0.7}$
J1324+2038a	$-17.9^{+1.4}_{-1.0}$	$12.20^{+0.07}_{-0.05}$	$14.1^{+3.6}_{-2.0}$	$13.8^{+1.1}_{-0.9}$	$11.32^{+0.37}_{-0.08}$	$4.2^{+13.3}_{-2.0}$
	$15.8^{+0.3}_{-0.3}$	$12.08^{+0.07}_{-0.04}$	$3.1^{+0.7}_{-0.8}$
J1324+2418a	$-24.5^{+0.7}_{-0.8}$	$11.97^{+0.04}_{-0.05}$	$6.6^{+1.4}_{-1.3}$	$-23.2^{+0.3}_{-0.3}$	$11.72^{+0.02}_{-0.03}$	$4.5^{+0.5}_{-0.5}$
J1325+2232aa	$-14.8^{+2.1}_{-1.6}$	$12.36^{+0.06}_{-0.07}$	$20.7^{+3.5}_{-3.1}$	$-26.1^{+0.4}_{-0.4}$	$11.71^{+0.03}_{-0.04}$	$6.3^{+0.8}_{-0.9}$
J1325+2232ab	$-17.3^{+0.3}_{-0.3}$	$12.19^{+0.02}_{-0.02}$	$9.7^{+0.6}_{-0.5}$	$-18.2^{+1.4}_{-1.6}$	$11.29^{+0.16}_{-0.11}$	$8.0^{+8.0}_{-3.1}$
J1332+2054a	$-11.5^{+1.1}_{-1.1}$	$11.57^{+0.03}_{-0.03}$	$3.2^{+0.8}_{-0.8}$	$-26.7^{+0.5}_{-0.5}$	$11.29^{+0.17}_{-0.10}$	$0.9^{+1.5}_{-0.4}$
	$-0.6^{+0.3}_{-0.3}$	$11.57^{+0.03}_{-0.03}$	$3.2^{+0.8}_{-0.8}$
J1335+2820a	$-24.2^{+0.5}_{-0.6}$	$12.35^{+0.03}_{-0.03}$	$11.3^{+0.9}_{-0.9}$
J1338+2345a
J1341+2801a	$-33.7^{+1.0}_{-0.9}$	$12.51^{+0.02}_{-0.02}$	$28.1^{+2.4}_{-1.6}$
J1341+2806a	$-72.6^{+4.4}_{-3.5}$	$12.42^{+0.15}_{-0.13}$	$35.4^{+19.1}_{-10.0}$
	$-26.2^{+1.9}_{-2.0}$	$12.46^{+0.04}_{-0.03}$	$35.8^{+5.2}_{-3.8}$
J1341+2823a	$-31.1^{+0.3}_{-0.3}$	$12.17^{+0.02}_{-0.02}$	$9.0^{+0.5}_{-0.5}$	$-32.2^{+0.1}_{-0.2}$	$12.00^{+0.21}_{-0.11}$	$0.9^{+0.2}_{-0.2}$
J1341+2824a	$-28.0^{+0.6}_{-0.5}$	$12.32^{+0.02}_{-0.02}$	$14.9^{+0.9}_{-0.8}$
J1341+2829a	$-27.5^{+0.4}_{-0.4}$	$12.39^{+0.02}_{-0.03}$	$7.6^{+0.6}_{-0.6}$
J1342+2828a	$-25.2^{+0.6}_{-0.5}$	$12.22^{+0.02}_{-0.02}$	$12.8^{+1.0}_{-0.9}$
J1344+1842a	$-24.2^{+0.2}_{-0.2}$	$12.38^{+0.01}_{-0.01}$	$14.1^{+0.5}_{-0.5}$	$-24.8^{+2.0}_{-1.2}$	$11.24^{+0.14}_{-0.09}$	$8.6^{+7.7}_{-3.1}$
	$-5.2^{+0.5}_{-0.6}$	$12.03^{+0.02}_{-0.02}$	$11.2^{+0.9}_{-0.8}$	$-3.5^{+0.2}_{-0.2}$	$11.68^{+0.02}_{-0.02}$	$2.7^{+0.6}_{-0.5}$
J1347+1811a	$-9.4^{+0.7}_{-0.6}$	$12.40^{+0.03}_{-0.03}$	$20.4^{+2.0}_{-2.0}$	$-1.8^{+0.3}_{-0.3}$	$11.74^{+0.02}_{-0.02}$	$6.6^{+0.7}_{-0.6}$
J1413+5621a	$-45.4^{+0.2}_{-0.2}$	$12.04^{+0.02}_{-0.02}$	$4.4^{+0.9}_{-1.0}$	$-45.6^{+0.1}_{-0.1}$	$12.07^{+0.07}_{-0.06}$	$1.5^{+0.2}_{-0.1}$
	$-4.8^{+1.0}_{-1.1}$	$11.88^{+0.04}_{-0.04}$	$12.6^{+1.9}_{-1.6}$	$-4.5^{+1.3}_{-1.2}$	$11.25^{+0.07}_{-0.07}$	$10.3^{+2.7}_{-2.2}$
J1415+3716a	$-36.9^{+0.8}_{-0.8}$	$11.57^{+0.05}_{-0.04}$	$6.9^{+1.5}_{-1.2}$	$-5.9^{+1.4}_{-1.7}$	$11.11^{+0.10}_{-0.10}$	$6.0^{+3.2}_{-2.6}$
	$-8.7^{+1.1}_{-1.0}$	$11.98^{+0.03}_{-0.03}$	$16.6^{+1.9}_{-1.9}$
J1420+5520a	$-11.6^{+0.6}_{-0.5}$	$11.82^{+0.04}_{-0.03}$	$7.9^{+1.6}_{-1.1}$
J1527+4027a	$-72.4^{+0.3}_{-0.3}$	$11.57^{+0.02}_{-0.02}$	$5.4^{+0.6}_{-0.6}$	$-3.0^{+0.1}_{-0.1}$	$11.55^{+0.02}_{-0.02}$	$2.6^{+0.4}_{-0.5}$
	$-54.7^{+0.5}_{-0.7}$	$11.31^{+0.06}_{-0.05}$	$5.0^{+1.6}_{-1.2}$
	$-28.2^{+0.3}_{-0.3}$	$11.46^{+0.03}_{-0.03}$	$4.5^{+0.7}_{-0.7}$
	$-6.5^{+0.2}_{-0.2}$	$12.08^{+0.01}_{-0.01}$	$9.6^{+0.3}_{-0.3}$
J1534+5015a	$-51.3^{+0.1}_{-0.1}$	$12.02^{+0.01}_{-0.01}$	$5.1^{+0.2}_{-0.2}$	$-30.9^{+0.2}_{-0.2}$	$11.81^{+0.01}_{-0.02}$	$4.4^{+0.3}_{-0.3}$
	$-28.4^{+0.04}_{-0.04}$	$12.90^{+0.03}_{-0.03}$	$4.1^{+0.1}_{-0.1}$	$-0.6^{+0.2}_{-0.2}$	$11.66^{+0.03}_{-0.02}$	$2.6^{+0.6}_{-0.6}$
	$-4.8^{+0.3}_{-0.3}$	$12.26^{+0.01}_{-0.01}$	$15.9^{+0.5}_{-0.4}$

Note. Properties of all Ca II and Na I gas absorption features measured along BHB sight lines. v_{LSR} is the measured radial velocity corrected for the local standard of rest in the direction of that sight line. log N is column density, and b_D is the Doppler b parameter of the absorption feature. Errors are the upper and lower quartiles determined by the MCMC line-fitting algorithm.

In order to isolate absorption features associated with Galactic inflows/outflows and examine their properties, we separate absorption lines into two distinct velocity components: “ISM” (velocities consistent with the Milky Way’s ISM, $|v| < 25 \text{ km s}^{-1}$)

and “IV” (IV gas, $|v| > 25 \text{ km s}^{-1}$). The first is a component we associate with the Milky Way ISM; this is gas moving within $\pm 25 \text{ km s}^{-1}$ of the LSR. Any gas outside this velocity range is not likely to be part of a coherent rotating disk and may be associated

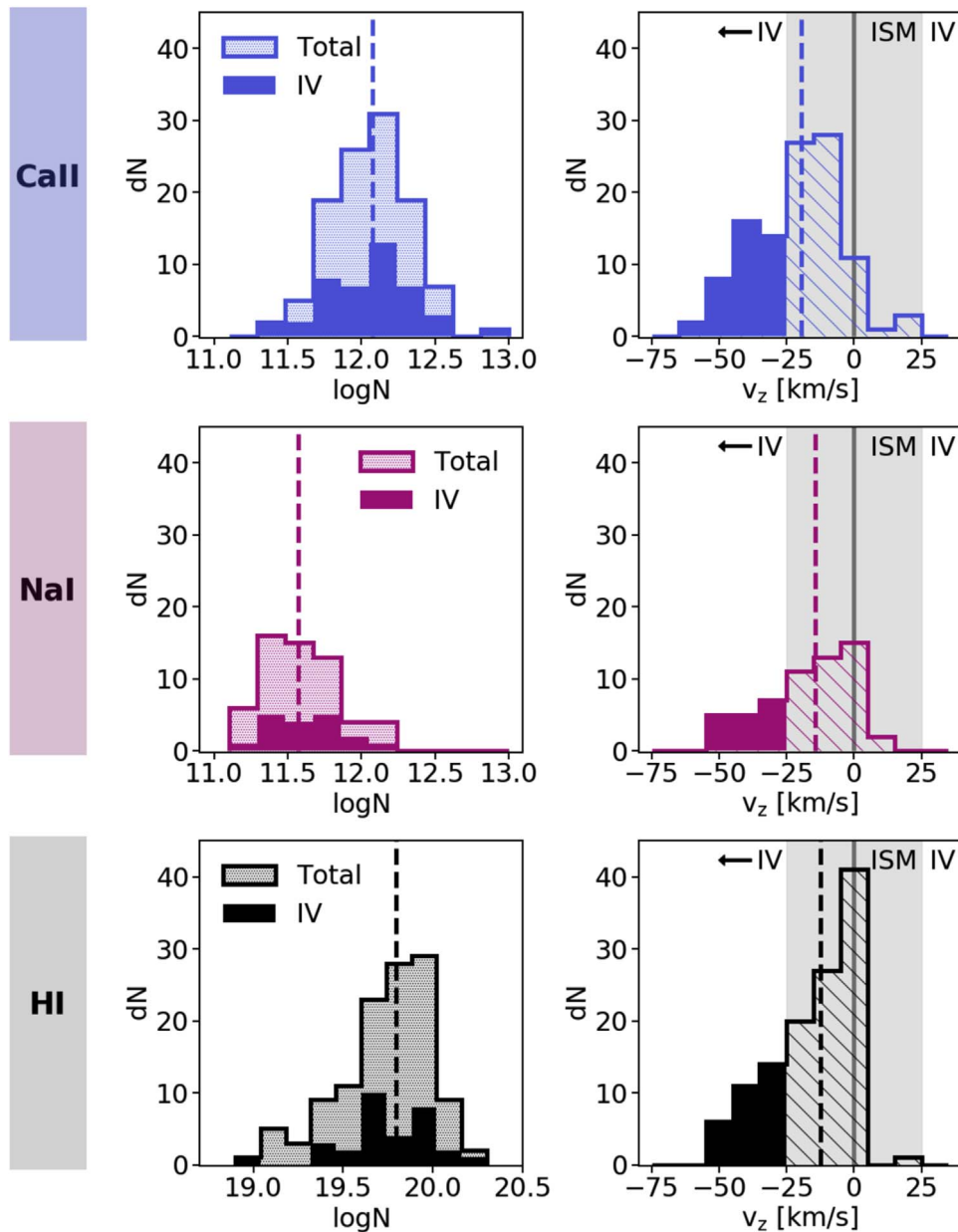


Figure 7. DISTRIBUTION OF COLUMN DENSITY AND VELOCITY. Measured column densities (left column) and the z -component of measured radial velocities (right column) for Ca II, Na I, and H I. Dashed lines mark the median value for each distribution, and in the right column $v_{\text{LSR}} = 0$ is indicated with a gray line. All ions are dominated by Galactic signals at $|v| < 25 \text{ km s}^{-1}$ (hatched histogram), but a significant IV component at $v < -25 \text{ km s}^{-1}$ can be clearly seen (filled histogram), indicating inflowing gas at the disk–halo interface.

with extraplanar gas flows. This so-called IV gas component is often defined as $35 \text{ km s}^{-1} < |v| < 90 \text{ km s}^{-1}$, but this range is somewhat arbitrary and the cutoffs are often adjusted based on the gas velocities of features being considered (van Woerden et al. 2005). In this work we do not detect any gas at $|v| > 75 \text{ km s}^{-1}$ and find that adopting a cutoff at $|v| = 25 \text{ km s}^{-1}$ for ISM gas best reveals the trends in these data.

It should be noted that interpretations of IV gas measurements are seldom clear-cut. At high Galactic latitudes, typical Milky Way disk gas should have low line-of-sight velocities, since the bulk of its motion is in the transverse direction. However, any extraplanar gas moving at $|v| < 25 \text{ km s}^{-1}$ cannot be easily disentangled from disk gas (Boettcher et al. 2017; Zheng et al. 2017).

4. Results

Table 2 lists best-fit values for column density N , radial velocity v , and Doppler b parameter b_D , which we combine with spatial coordinates from the SEGUE catalog to provide a characterization of IV gas in the halo. Figure 7 shows the distribution of the Ca II, Na I, and H I parameter values fit using the methods described in Section 3.1.

We have tabulated results for gas detections at all velocities but limit discussion in the body of this paper to the IV gas component. The results and figures for the Milky Way ISM component ($|v| < 25 \text{ km s}^{-1}$) are presented in Appendix A. This low-velocity gas behaves largely as expected for typical disk material, but we examine some noteworthy features of this component as they relate to IV gas.

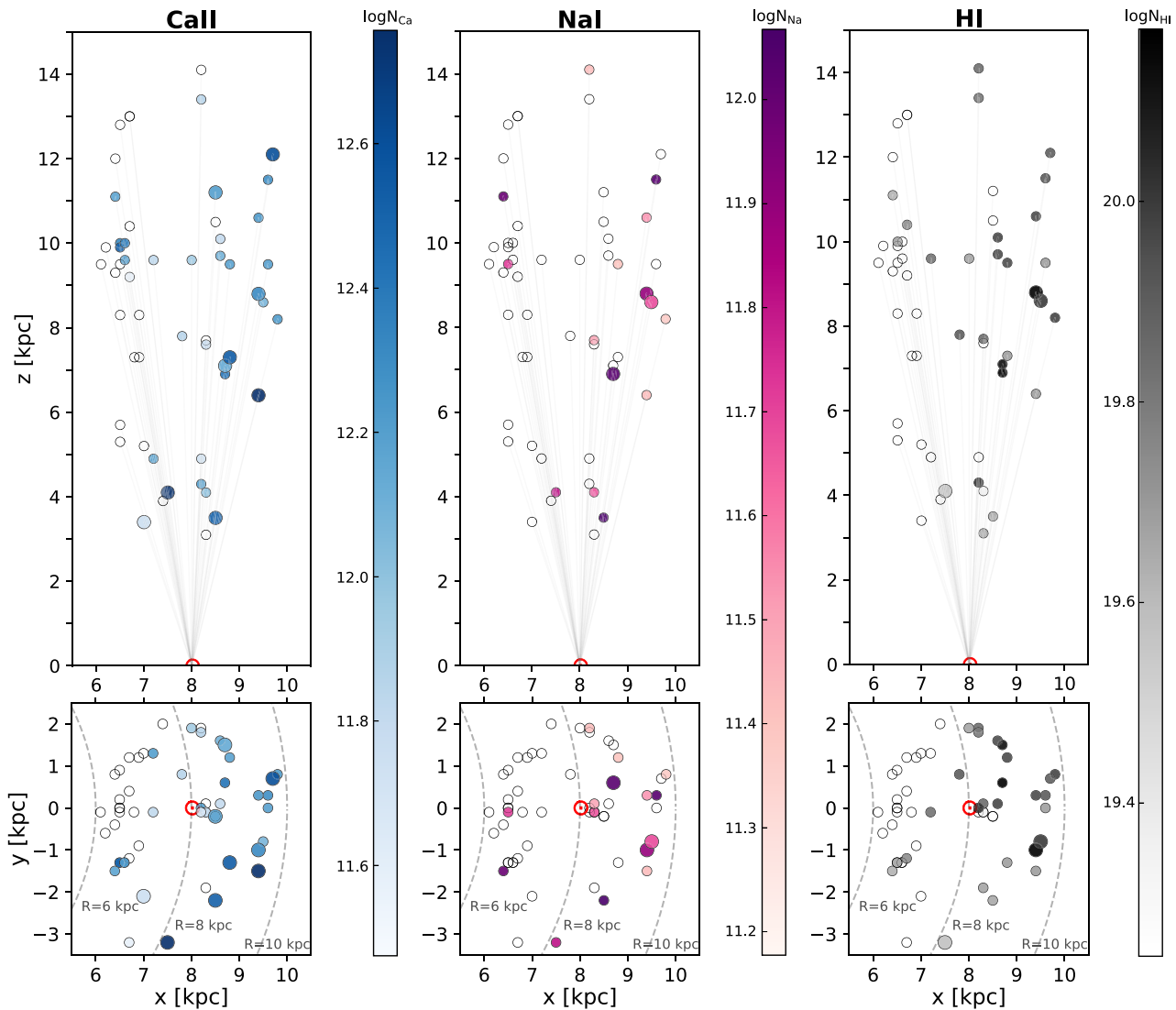


Figure 8. COLUMN DENSITY MEASUREMENTS ALONG BHB SIGHT LINES. Column densities for the IV component (IV gas, $v < -25$ km s $^{-1}$). Markers correspond to background BHB sight lines projected onto the x - y and x - z planes of the Milky Way disk. The coordinates for each BHB are plotted in physical kpc units in the plane of the Milky Way; thus, any inferred distance to gas absorption along a sight line is an upper limit. Color indicates column density measurements for Ca II and Na I in absorption and H I in 21 cm emission. Larger markers indicate sight lines along which more than one component was detected, and their colors represent the total column density of those components. Open circles denote nondetections. The Sun is marked by a red solar symbol, and black dashes denote lines of constant radius from Galactic center. IV column densities do not uniformly increase with z or BHB distance, implying that most of the gas is closer than the nearest background source at $z \lesssim 3.1$ kpc.

4.1. Column Density

Absorption-line measurements reveal how gas column densities vary across the face of the Milky Way’s disk. When these measurements are combined with distances to background BHBs, we can also see how column densities vary with height above the disk, providing a 3D picture of the absorbing gas. Figure 8 shows total column densities for the IV gas component along each sight line, both from an edge-on view (top panel) and projected onto the plane of the Milky Way’s disk (bottom panel). The markers are located at the coordinates of the background BHB; in other words, they reflect the upper limit on distance to the absorbing Ca II and Na I gas. Results remain qualitatively the same if smaller distances are assumed (see Figure 4 for an example of the effect of distance assumptions on gas cloud coordinates). Colors indicate the column density of IV gas, with darker colors corresponding to greater column densities and open circles denoting nondetections. Larger markers represent sight lines with multiple

distinct IV gas components that have each been fit separately, and their colors represent the summed column density of those components.

In the x - y plane, most detections of IV gas are grouped together along sight lines outside the solar circle, while very little IV gas is found in the direction toward the Galactic center. This pattern is consistent across the Ca II, Na I, and H I tracers. Although Ca II and H I detections appear spatially coincident, we find no significant correlation between Ca II and H I column densities as one might expect (Pearson $r = -0.04$, $p = 0.86$). We speculate that this may be an effect of the 10’/8 beam size of the EBHIS H I data, which smears out signal over a large area relative to the 1’’ slit width for HIRES. Alternatively, the absence of any correlation in Ca II–H I column density could be real if the H I is associated with gas in a more highly ionized phase.

Additionally, there is no significant correlation between column densities and the height probed by a sight line. This absence of any trend between total column density along a

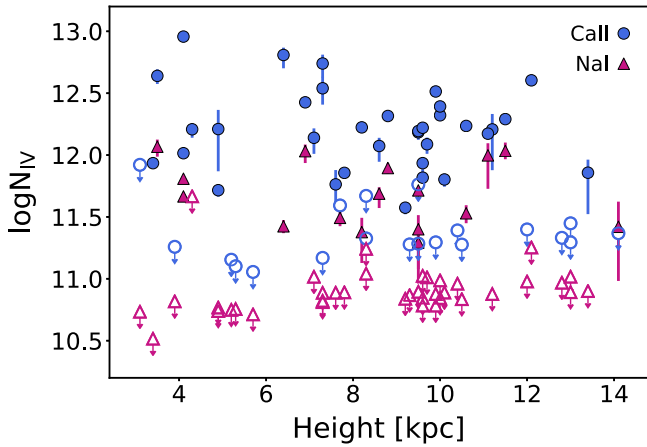


Figure 9. CA II AND NA I LIE CLOSE TO THE DISK. The total column density of IV gas detected along BHB sight lines, which have background sources at varying heights above the disk. Ca II measurements are marked by blue circles, and Na I measurements by magenta triangles. For sight lines along which no gas was detected, 2σ upper limits on column density are shown with open symbols. There is no correlation between the distance probed by a sight line and the total column density of gas, suggesting that most of the gas detected lies closer than the nearest background source at $z \lesssim 3.1$ kpc.

sight line and the height of the background source above the disk can be seen more clearly in Figure 9. If the gas were distributed uniformly or exhibited a smooth drop-off with height, we would expect to observe higher column densities along sight lines to more distant background sources. We find no evidence of such correlation (Pearson $r = -0.09$, $p = 0.64$), an indication that most of the observed gas lies at a distance closer than $z = 3.1$ kpc, the distance to the nearest background source. Further support for this picture can be seen in Figure 10, in which our Ca II IV gas column density measurements are overlaid on a map of HI column density from the LAB survey (Kalberla et al. 2005). These Ca II detections visibly coincide with the edge of two large HI complexes called the IV Arch and the IV Spur, which extend across much of the northern Galactic sky and are estimated to sit above the Galactic disk at distances of 0.5–3 kpc (Kuntz & Danly 1996; Wakker 2001; Smoker et al. 2011).

4.2. Kinematics

Figure 11 maps infall velocities for the IV gas component, again both from an edge-on view (top panel) and projected onto the plane of the Milky Way’s disk (bottom panel). Colors represent the z -component of measured radial velocities ($v_z = v \sin b$) in order to show motion directly toward/away from the disk. This survey has been designed to optimize constraints on the vertical component of gas velocities, so transverse velocities are not shown because they are not well constrained by our experiment. However, results do not differ significantly if the observed radial velocity is used instead. Larger markers indicate sight lines with multiple distinct IV absorption features, and their colors represent the $\log N$ -weighted mean velocity of those components. A plus sign marks the location of two positive-velocity absorbers just beyond the 25 km s^{-1} IV cutoff in Ca II and HI for J1223+0002a, and another in Ca II at 40.8 km s^{-1} for J1258+1939. These absorption features are shown in Appendix B, and the parameters of their line profile fits are listed in Table 2. The distance constraints on our sight lines allow us to look at gas

velocities in a unique way by projecting measured velocities on the x - y plane of the disk. As in the corresponding column density plot (Figure 8), the location of each point reflects the upper limit on distance to the absorber, which lies somewhere between the background star and the Sun. The location of the Sun is indicated with a red symbol, and dashed lines indicate lines of constant radius from the Galactic center.

The IV component we have isolated reveals a distinct pattern in vertical infall velocity. Virtually all of the IV gas within 13 kpc is at negative velocities, falling toward the disk. We detect only two IV Ca II absorbers at positive velocities and a single positive-velocity HI IV absorber just beyond the ISM velocity cutoff ($v = 25 \text{ km s}^{-1}$). This is consistent with previous findings that gas in this HI complex, as well as the vast majority of IV gas at northern Galactic latitudes, is moving toward the disk (Kuntz & Danly 1996; Albert & Danly 2004; Richter 2017). We find no correlation between velocity and height above the disk; this provides further support for the picture suggested by our column density measurements in which IV gas sits mostly close to the disk at small heights (see Section 4.1). Furthermore, we find no correlation between velocity and column density (see Figure 12).

IV gas does exhibit a clear infall velocity gradient across the face of the disk, which is oriented roughly along the radial axis of the Milky Way. Gas infall velocities at $R = 6$ – 10 kpc increase in magnitude farther from the Galactic center ($-6.0 \pm 1.5 \text{ km s}^{-1} \text{ kpc}^{-1}$ in Ca II, $-7.0 \pm 1.7 \text{ km s}^{-1} \text{ kpc}^{-1}$ in Na I, and $-8.8 \pm 1.3 \text{ km s}^{-1} \text{ kpc}^{-1}$ in HI). This velocity gradient is especially prominent for Ca II and HI, as seen in the bottom panel of Figure 11. A similar trend appears in Na I, although there are fewer Na I detections overall. The gradient spans velocities from the IV cutoff at -25 to -75 km s^{-1} , with faster-moving gas detected near the interior of the coincident HI IVCs mentioned in Section 4.1. In Figure 13, least-squares linear fits to this gradient for Ca II, Na I, and HI show that this gradient is not explained by a geometric viewing effect, which would cause the z -component of observed radial velocities to be smaller for sight lines at lower Galactic latitudes, not larger.

The Ca II velocity measurements are overlaid on a map of flux-weighted HI velocities from the LAB survey (Kalberla et al. 2005) in Figure 14. As mentioned above and shown in Figure 10, Ca II gas detections coincide with a large HI IVC complex, probing an area at the edge of the well-studied IV Arch and IV Spur. The locations of our Ca II detections in the x - y plane are spatially coincident with that HI structure and have similar velocity gradients. However, the Ca II column densities and HI column densities are not correlated, which may be a result of mismatched spatial scales probed by emission and absorption observations, respectively. Such properties of HI and Ca II may indicate that large coherent structures are accreting onto the Milky Way in a manner more complex than a single-slab accreting layer (Zheng et al. 2017; Forbes & Lin 2018). We explore various galactic fountain scenarios in Section 5.2.

4.3. Cloud Size and Distribution

Given that the majority of detections are grouped together at $x \gtrsim 8$ kpc, it is likely that we are mapping the edge of a large structure >3 kpc in extent. Such an extended structure may be composed of many smaller gas cloud fragments or filaments that effectively provide uniform coverage, as is the case for some HVCs (Wakker 2001; Putman et al. 2002; Stanimirović

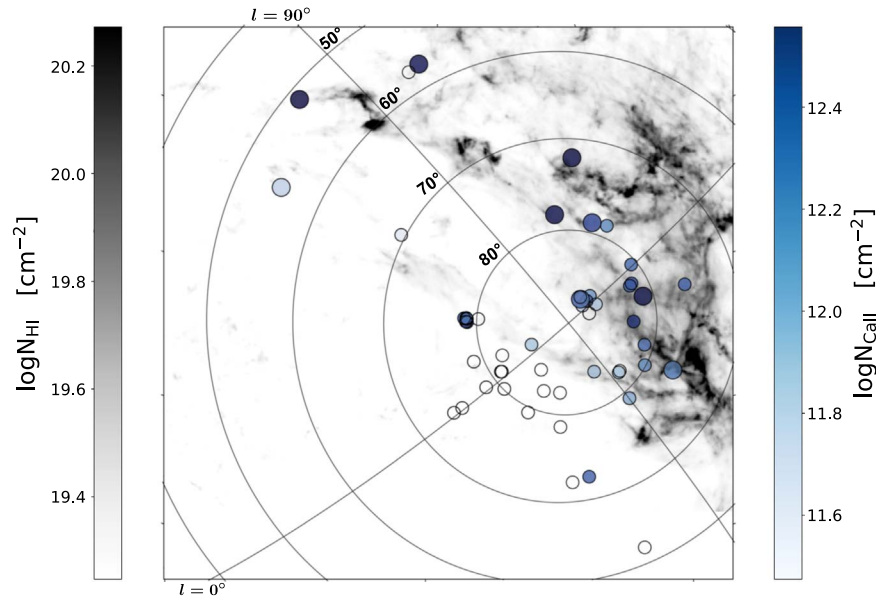


Figure 10. CA II COLUMN DENSITY COMPARISON TO H I 21 CM MAP. A map of H I column density at $-60 \text{ km s}^{-1} < v < -25 \text{ km s}^{-1}$ from the LAB survey in gray (Kalberla et al. 2005), overplotted with Ca II IV gas column densities from this work in blue. Each marker represents a BHB sight line, colored by the total IV gas column density along that sight line. Open circles denote nondetections. Larger markers indicate sight lines with multiple distinct IV absorption components and are colored by the total IV column density of those components. Ca II detections correlate with cool gas near the edge of two large H I complexes known as the IV Arch and the IV Spur.

et al. 2008; Hsu et al. 2011). The substructure created by these so-called clouds is probably composed of many interrelated clumps and wisps, rather than discrete structures with well-defined boundaries (Ben Bekhti et al. 2007; Marinacci et al. 2010; Fukui et al. 2018; McCourt et al. 2018).

Comparing Ca II and Na I detections to existing H I maps provides further support for wispy substructures within clouds that extend beyond the coverage of this survey. Figure 10 shows H I emission from the LAB survey in gray, and such morphology is clearly visible (Kalberla et al. 2005). Our IV gas detections correlate strongly with the IV Arch and IV Spur H I complexes that extend across much of the northern Galactic sky and contain clumpy substructures with angular sizes of 10° – 20° (Kuntz & Danly 1993).

Distance estimates for the H I IV Arch and Spur generally fall within a range of 0.5–3 kpc (e.g., Kuntz & Danly 1996; Wakker 2001; Smoker et al. 2011), which is consistent with the distance constraint of $z \lesssim 3.1$ kpc we have determined for detected gas in this sample. If low-ionization Ca and Na can be tied to H I IVCs close to the disk, then measurements of H I gas provide additional spatial constraints. To illustrate this, Figure 4 maps the x – y coordinates of gas assuming a cloud at $z = 3$ kpc, compared to the x – y coordinates corresponding to the upper limit on distance set by the background star. We assume a cloud height of $z = 3$ kpc for the purposes of demonstration, since our detections place only an upper limit on this value. This figure highlights the significant effect that distance measurements can have on our ability to constrain substructure and cloud size. Connecting Ca II and Na I gas with H I lying close to the disk is therefore a useful link that allows us to place tighter constraints on the scale of structures within the larger cloud probed by this survey.

Statistical variations in column density can also provide constraints on the size of gas clouds and the uniformity of their

coverage across the disk (Rubin et al. 2018a, 2018b). To show how column densities vary on different scales, we plot the difference in IV gas column density, $\Delta \log N_{\text{Ca II}}$, between each unique pair of sight lines in Figure 15. Na I and H I are not shown, but the results for those species are similar to Ca II. We assume that the gas lies at a height of 3 kpc, as suggested by the trends discussed above. Figure 4 provides an example of how the distance scales in question are affected for a range of assumed cloud heights.

In the top panel, each marker represents the difference in column density for two sight lines separated by some physical distance. Pairs of sight lines with two detections (d–d) are represented with filled teal markers. Pairs with one detection and one nondetection (nd–d) are represented by open gold markers showing the lower limits on $\Delta \log N$ as determined by instrumental detection limits. The gray bars at the bottom of the plot show the physical separation of sight-line pairs with two nondetections (nd–nd). If the spatial sampling density of our sight lines is high enough to probe cloud substructure, we would expect $\Delta \log N$ to be smaller at pair separations less than the characteristic clump size. We find that column densities differ by up to two orders of magnitude, but there is no strong evidence of density fluctuations on any particular physical scale.

The histogram in the middle panel displays the distribution of sight-line pair separations. The full set of all sight-line pairs is in black, d–d pairs in teal, nd–d pairs in gold, and nd–nd in dashed gray. Note that the distribution of d–d pairs is skewed relative to the total distribution of sight-line pairs. We expect the number of d–d pairs to increase on scales smaller than typical gas structure. The bar graph in the bottom panel represents the ratio of the number of d–d pairs to nd–d pairs corresponding to each bin of the histogram above. The ratio is normalized so that it is positive when there are more d–d pairs and negative when there are more n–d pairs. At scales shorter

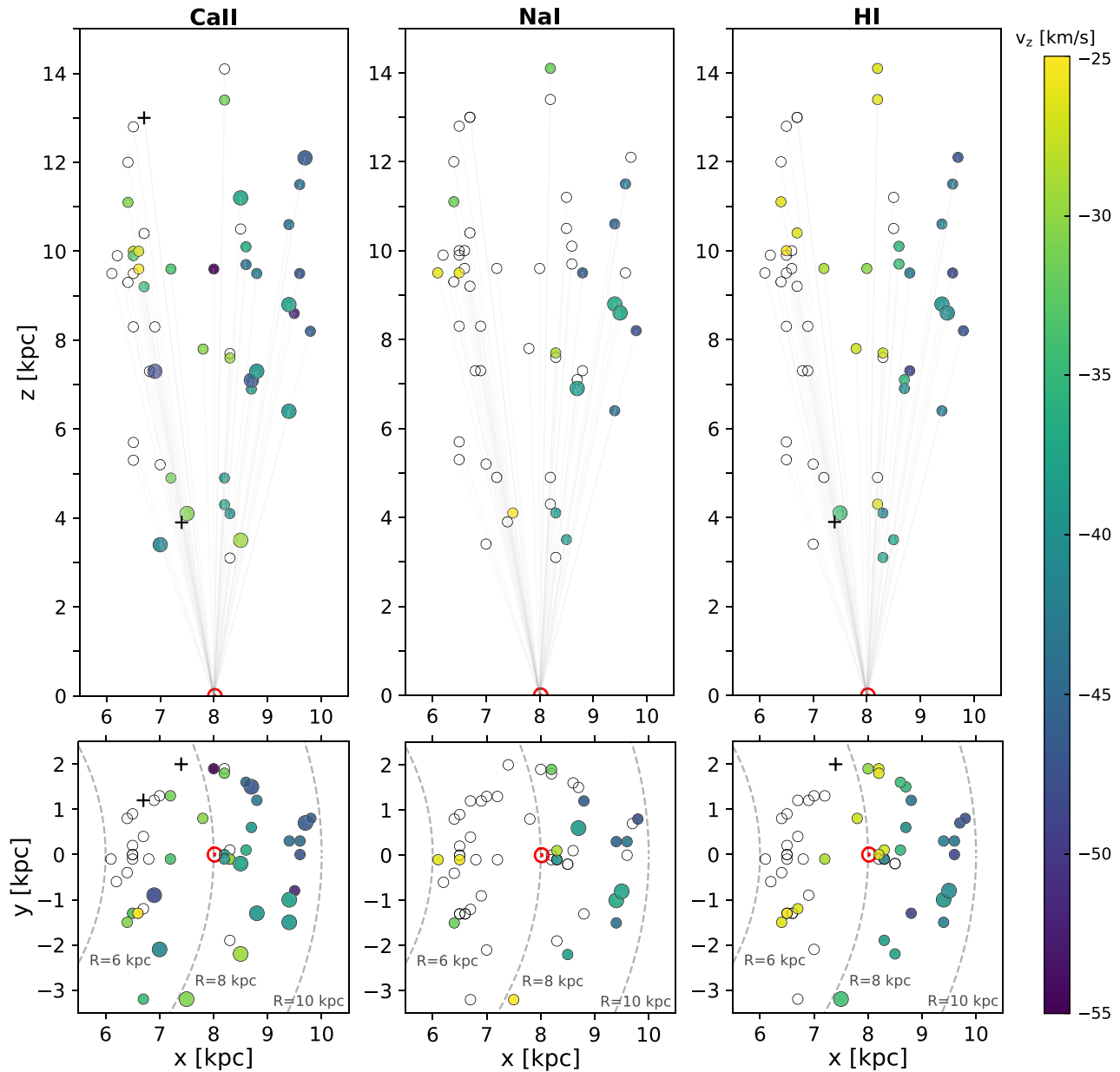


Figure 11. INFALL VELOCITY MEASUREMENTS ALONG BHB SIGHT LINES. Infall velocities for the IV component (IV gas, $v < -25 \text{ km s}^{-1}$). Markers correspond to background BHB sight lines projected onto the x - z (top) and x - y (bottom) planes of the Milky Way disk. The coordinates for each BHB are plotted in physical kpc units in the plane of the Milky Way; thus, any inferred distance to gas absorption along a sight line is an upper limit. Color indicates the component of radial velocity measurements perpendicular to the disk ($v_{\text{LSR}} \sin b$) for Ca II and Na I in absorption and H I in 21 cm emission. Larger markers indicate sight lines along which more than one component was detected, and their colors represent the mean velocity of those components weighted by column density. IV gas is only detected at negative velocities, with the exception of one absorber just beyond the IV cutoff in Ca II and H I, and another at $v = 40.8 \text{ km s}^{-1}$ in Ca II. These absorbers are marked by a plus sign. Open circles denote nondetections. The Sun is marked by a red solar symbol, and black dashes denote lines of constant radius from Galactic center. The infalling gas exhibits a clear velocity gradient, especially in Ca II. By comparison, the “ISM” gas shows no such trend (see Appendix A).

than 0.5 kpc, there are more d-d pairs than nd-d pairs, and there is an inversion of this ratio at scales larger than 0.5 kpc.

The absence of a trend at separations larger than 0.5 kpc is an indication that any existing substructure occurs at scales no larger than 0.5 kpc, approximately twice the average separation between a sight line and its nearest neighbor (0.24 kpc). Similarly, large-scale cloud structures are likely to span areas larger than the $\sim 12.6 \text{ kpc}^2$ covered by this survey. These constraints are consistent with the H I gas structure shown in Figure 10, where dense clumps have formed on scales smaller than our typical sight-line separation and make up a cloud complex that extends beyond the survey area.

4.3.1. Covering Fraction and Volume Filling Factor

We calculate covering fraction as a convenient and simple measure of the projected sky coverage and distribution of IV gas. Before proceeding with the calculation, we must recognize that our sight lines extend to varying distances, and this should be taken into account. In this case, we assume that the detected gas lies at $z = 3 \text{ kpc}$ and therefore all sight lines fully probe these gas clouds, and we assert that this is a valid assumption based on the argument laid out in Section 4.1. See Figure 4 for an illustration of the effect of cloud height assumptions on distance scales.

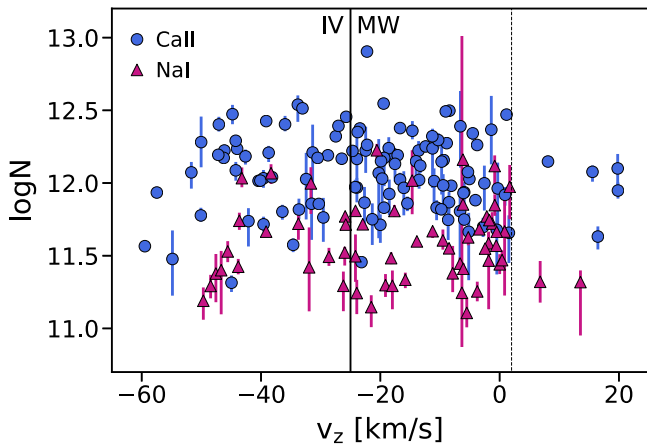


Figure 12. COLUMN DENSITY AND VELOCITY ARE UNCORRELATED. Column density and z -component velocity for all distinct IV absorption components. Ca II measurements are marked by blue circles and Na I by magenta triangles. There is no apparent relationship between the column density of the gas and its infall velocity. Note the abrupt drop-off in Ca II and Na I detections at $v_z \gtrsim 2 \text{ km s}^{-1}$, marked by the vertical dotted line. This dearth of cool gas at positive velocities is also present in H I.

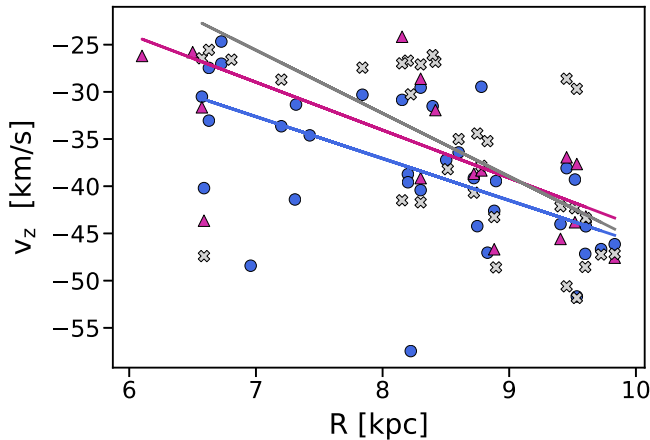


Figure 13. A VELOCITY GRADIENT ACROSS THE DISK. IV gas velocities for Ca II and Na I detections in absorption and H I 21 cm emission, showing the z -component of measured radial velocity as it varies with distance from Galactic center. For sight lines with more than one IV component, the log N -weighted velocity is shown. Lines show the least-squares fit to the data, revealing velocity gradients of $-6.0 \pm 1.5 \text{ km s}^{-1} \text{ kpc}^{-1}$ in Ca II, $-7.0 \pm 1.7 \text{ km s}^{-1} \text{ kpc}^{-1}$ in Na I, and $-8.8 \pm 1.3 \text{ km s}^{-1} \text{ kpc}^{-1}$ in H I.

We must also choose a column density threshold above which the covering fraction will apply. Column density measurements are a mix of detections and upper limits representing nondetections. Ideally there should be no upper limits above the chosen threshold, since this does not allow us to categorize that sight line definitively as a detection or nondetection. However, choosing a threshold that meets this criterion would exclude a significant fraction of detections in our sample (see Figure 9). In light of this, we take the following approach: We choose a threshold of $\log N_{\text{IV}} > 11.5$ for Ca II, which includes all detections and exceeds all but four upper limits, and a threshold of $\log N_{\text{IV}} > 11.3$ for Na I, which includes all detections and exceeds all but one upper limit. We treat the upper limits that exceed the threshold as detections and account for this uncertainty in the covering fraction error. The covering fraction error is determined by a standard binomial Wilson score; we calculate the 68% confidence interval treating

the upper limits above the threshold as both detections and nondetections and report the most conservative of those two values.

Using 54 sight lines, we calculate covering fractions of $f_{\text{Ca II}} (\log N_{\text{Ca II}} > 11.5) = 63_{-14.0}^{+6.5} \%$, $f_{\text{Na I}} (\log N_{\text{Na I}} > 11.3) = 26_{-7.6}^{+5.9} \%$, and $f_{\text{H I}} (\log N_{\text{H I}} > 18.7) = 52\% \pm 5.8\%$. Other studies of neutral H I clouds in the Milky Way have found smaller covering fractions of $\sim 20\%$ – 40% (Wakker & van Woerden 1991; Murphy et al. 1995; Albert & Danly 2004). Studies of warm HVCs in the Milky Way halo find covering fractions of $\sim 60\%$ – 90% , larger than the low-ionization covering fractions we measure (Collins et al. 2009; Shull et al. 2009; Lehner & Howk 2011).

If we use our statistical analysis in Section 4.3 to make an assumption about cloud size, we can also calculate the volume filling factor, given by

$$F = N_c \frac{\frac{4}{3}\pi r_c^3}{\pi R_s^2 z}. \quad (1)$$

N_c is the total number of IV components detected along all sight lines, including six sight lines with two IV components and one sight line with three IV components. We assume that each IV gas detection is a distinct spherical cloud substructure and that the size of these structures must be smaller than the scales we probe with this survey given the absence of statistical variation in column density described in Section 4.3. We assign an upper limit of $r_c \leq 0.1225 \text{ kpc}$ on cloud radius using the average xy -projected distance between a sight line and its nearest neighbor (0.245 kpc). $\pi R_s^2 = 12.6 \text{ kpc}^2$ is the disk area covered by the cylindrical survey volume, and we assume the height of that cylinder to be $z = 3 \text{ kpc}$ since we find no evidence of IV gas at $z > 3 \text{ kpc}$. This gives us volume filling factors of $F_{\text{Ca II}} (\log N_{\text{Ca II}} > 11.5) \leq 0.86_{-0.15}^{+0.07} \%$, $F_{\text{Na I}} (\log N_{\text{Na I}} > 11.3) \leq 0.35_{-0.08}^{+0.06} \%$, and $F_{\text{H I}} (\log N_{\text{H I}} > 18.7) \leq 0.63\% \pm 0.06\%$.

Although these volume filling factors are quite small compared to the covering fraction we calculate ($F_{\text{Ca II}} \leq 0.28\%$ vs. $f_{\text{Ca II}} = 63\%$), the values are not contradictory if cloud sizes are small, as suggested by our analysis of column density fluctuations in Section 4.3. Even for length scales as short as $\sim 1 \text{ kpc}$ the covering fraction of small clouds easily reaches unity, which can explain the high detection rates of low-ion CGM gas if it does in fact clump on scales $< 500 \text{ pc}$ (Liang & Remming 2018).

5. Discussion

5.1. Implications of Small Cloud Size

The larger covering fractions and volume filling factors we see for higher ionization states support a multiphase picture in which small clumps or droplets of cool gas are suspended within larger clouds or streams of hotter, more diffuse gas. How this gas eventually cools and becomes incorporated into the ISM remains controversial. At $T \sim 10^6 \text{ K}$, thermal line emission can rapidly cool gas until it reaches $T \sim 10^4 \text{ K}$, where the cooling curve drops off steeply (Sutherland & Dopita 1993; Maio et al. 2007). Maller & Bullock (2004) argue that thermal instabilities naturally arise in the Galactic corona in which cool clouds condense from a hot medium, while Binney et al. (2009) have pointed out that the halo, under most assumed physical conditions, is largely stable to cooling. Instead, it may be that feedback-induced or fountain-induced cooling, in which metal-enriched clouds ejected from the disk mix with coronal

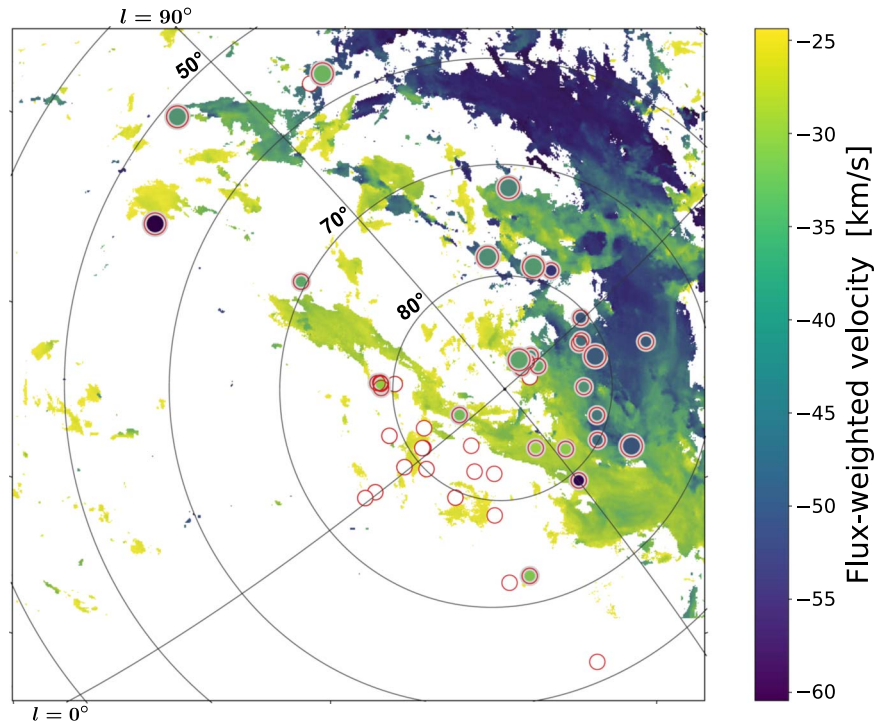


Figure 14. CA II VELOCITY COMPARISON TO H I 21 CM MAP. Map of flux-weighted H I velocities at $-60 \text{ km s}^{-1} < v < -25 \text{ km s}^{-1}$ from the LAB survey (Kalberla et al. 2005), overplotted with column-density-weighted infall velocities of Ca II from this work. Each marker represents a BHB sight line, colored by the velocity of IV gas along that sight line. Open circles denote nondetections. Larger markers indicate sight lines with multiple IV absorption components at distinct velocities, and their color represents the mean velocity of those components weighted by column density. Ca II detections correlate with the edge of two large H I complexes known as the IV Arch and the IV Spur. A velocity gradient can be seen in Ca II, with faster infall velocities nearest the interior of the cloud.

material and enhance the subsequent cooling, are the relevant processes driving accretion at the disk–halo interface (Marinacci et al. 2010, 2012; Fraternali 2017; Howk et al. 2018). Detailed, global hydrodynamic disk simulations will be critical to resolving the physics of gas accretion and the Galactic fountain (e.g., Fielding et al. 2017; Kim & Ostriker 2018; Schneider et al. 2018).

The largely empirical picture of cooler, denser gas embedded within warmer, more diffuse clouds may provide insight as to why we have sparser detections in Na I, which predominantly traces dust and dense-neutral gas ($T \lesssim 1000 \text{ K}$), than in Ca II, which traces both dense-neutral and warmer ionized gas ($T \lesssim 10,000 \text{ K}$), despite the fact that our sensitivity to both is roughly the same (Puspitarini & Lallement 2012; Murga et al. 2015). If Na I clouds sit within larger Ca II clouds in such a hierarchical structure, then some random sight line is less likely to pass through the Na I cloud (Stern et al. 2016). More generally, if the cold phase of CGM gas lies in small, clumpy structures rather than diffuse clouds that fill a larger volume in warm phase gas, then low-ionization clouds must be relatively common in order to explain the detection rates we see.

Currently, most galaxy simulations can resolve scales of $\sim 500 \text{ pc}$ at best and usually do not focus computational resources on resolving low-density gas in the CGM. In general, these simulations underpredict the amount of observed CGM ions (e.g., Hummels et al. 2018; Peeples et al. 2019). Incorporating AGN feedback has improved predictions of high ion abundances, but simulations still struggle to reproduce low ion abundances, even for hydrogen (Oppenheimer et al. 2018). If low-ion CGM clouds do form on scales $< 500 \text{ pc}$ as our analysis and those of others suggest, then the resolution of CGM gas in simulations must increase by orders of magnitude

in order to reflect the hydrodynamics on relevant scales (Marinacci et al. 2010; Crighton et al. 2015; Liang & Remming 2018; McCourt et al. 2018; Sparre et al. 2019). Recent work has demonstrated that improving resolution to $< 500 \text{ pc}$ in simulations dramatically changes the characteristics of cool gas clouds (Hummels et al. 2018; Peeples et al. 2019). As simulations improve and move closer to resolving these structures on stabilization scales, observational constraints on cloud properties like the ones we present here will be useful for testing the accuracy of their predictions.

5.2. Gas Origins and the Galactic Fountain

The galactic fountain broadly depicts a scenario in which hot gas is ejected from a galaxy by energetic feedback processes associated with star formation and/or a central supermassive black hole and then reaccrues onto the disk to catalyze new star formation in an ongoing cycle. Our findings indicate a substantial amount of cool extraplanar gas embedded within neutral structures moving toward the disk at distances less than 3.1 kpc . The observed bulk kinematics presented in this study provide clues about the origin and fate of gas at the disk–halo interface. In this section we consider our observations in the context of the “galactic fountain” and the potential origins of neutral infalling gas. In particular, we examine how the data might be explained by gas ejected from elsewhere within the Milky Way: either by star formation processes throughout the disk or driven by a central galactic engine. A viable model should be able to reproduce the velocity gradient and lack of column density trends we observe.

One well-established picture of the galactic fountain places the origin of infalling gas at the sites of supernova explosions throughout the disk. Fraternali (2017) models several variations

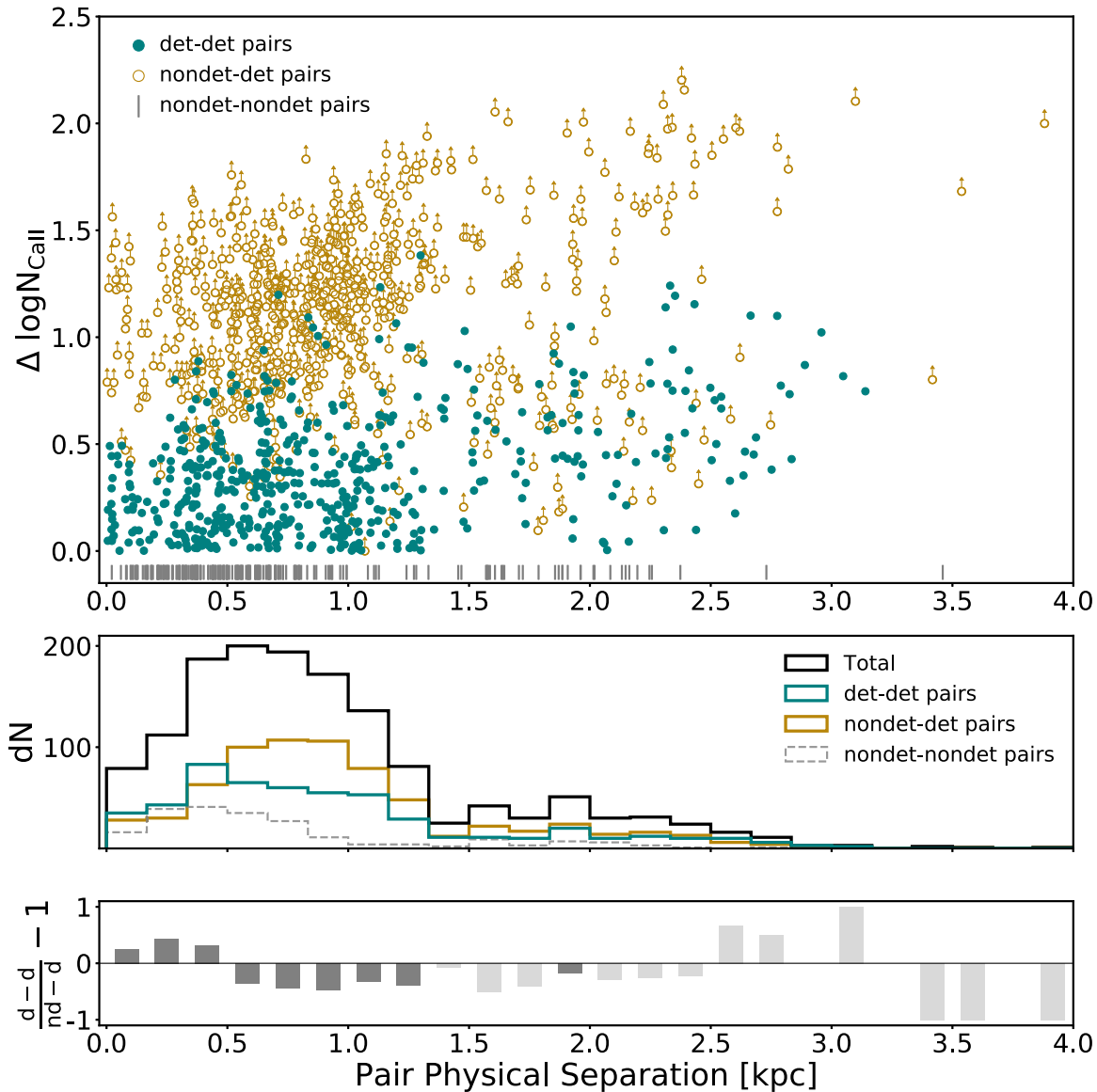


Figure 15. COLUMN DENSITY VARIATIONS INDICATE CLOUD SIZES < 500 PC. The spatial variation of $\log N$, which can place constraints on gas cloud size. The physical separation between IV gas along each unique pair of sight lines is calculated assuming that all gas lies at $z = 3$ kpc. Top: filled teal markers represent the difference in Ca II column density of gas between two sight lines with Ca II detections (d-d). If one sight line in the pair is a detection and one a nondetection (nd-d), lower limits on $\Delta \log N$ are determined by instrumental detection limits and indicated with an open gold marker. If both sight lines in a pair are nondetections (nd-nd), their physical separation is marked with a gray bar at the bottom of the figure. Middle: the distribution of sight-line pair separations is shown in the histogram at the top of the figure. The full set of all sight-line pairs is in black, d-d pairs in teal, nd-d pairs in gold, and nd-nd in dashed gray. Bottom: ratio of the number of d-d pairs to nd-d pairs for each bin of the histogram above. The ratio is normalized so that it is positive when there are more d-d pairs and negative when there are more nd-d pairs. Light-gray bars are shown for bins in which there are fewer than 50 sight-line pairs. Below scales of 0.5 kpc, there are more d-d pairs than nd-d pairs, and there is an inversion of this ratio at scales larger than 0.5 kpc. This may be an indication that there is gas substructure at scales on the order of 0.5 kpc.

of the disk-ejection fountain scenario that could produce the velocity gradient we see: in a simple ballistic model, particles ejected vertically from the disk will fall back to the disk at larger radii because of conservation of angular momentum. Since gravitational potential decreases with galactic radius, ejecta at larger radii will reach a greater height. In turn, this material will reach more negative velocities by the time it reaches the disk. Such an effect could produce a radius-dependent infall velocity gradient for cooled, infalling gas. Adding in effects of condensation and drag could mean that these particles also return to the disk at significantly smaller radii. Our data can be explained by a disk-ejection scenario if outflowing gas is in a hotter phase that is difficult to detect with low ion absorption, or if the outflows are time variable over

many megayears as a result of intermittent, clustered star formation, as in the models of Kim & Ostriker (2018). Although cool outflowing gas has been detected in other local galaxies (Heckman et al. 2000; Martin 2005; Rupke et al. 2005; Chen et al. 2010; Bordoloi et al. 2014a; Rubin et al. 2014), such outflows may have a patchy distribution across the disk, over which our observations span only a small fraction.

The velocity gradient we observe across the disk could potentially emerge in a central engine scenario as well (Fox et al. 2015; Bordoloi et al. 2017). In this picture, gas is driven out from the center of the galaxy in a roughly conical region extending above the disk. Gas clouds cooling and condensing at the boundary of the cone at higher galactic radii would also be at greater height above the disk. This would allow gas

clouds at greater radii to reach greater velocities by the time they reach the disk–halo interface. The effect would be a similar radius-dependent velocity gradient to the one described for the disk-ejection scenario above, but through a different mechanism. Over time the trajectory of this infalling gas turns toward the potential well at galactic center and begins to move more quickly across the plane of the disk, which is consistent with a lack of detected outflows in the solar neighborhood. Gas clouds that condense further from galactic center would have longer infall times and therefore experience a greater trajectory change, leading to a decrease in z -component velocities as they fall and turn toward galactic center. Although this observed phenomenon emerges nicely in a simple toy model of this scenario, it does not easily reproduce gas that predominantly lies at small z unless a full opening angle of $\phi > 110^\circ$ is adopted for initial gas ejection. A larger sample of halo star sight lines over the full sky would be necessary to fully test this proposed scenario.

In principle, the metal abundance of the clouds we observe could also place constraints on its origin. Gas with low metal abundance may have originated from the IGM or been stripped from the ISM of Milky Way satellite galaxies (Kirby 2011). Larger metal abundances would suggest that material has been processed through stars in the disk and ejected via outflows as part of a galactic fountain. Furthermore, the differing elemental yields of sources like supernovae, stellar winds, or AGNs could potentially be tied to the relative abundances of various species across timescales of ~ 100 – 300 Myr (Emerick et al. 2018; Krumholz & Ting 2018). Unfortunately, determining the metal abundance for the extraplanar gas we observe is overall a very problematic calculation, and our data do not independently constrain the gas metallicity because of the lack of HI in absorption. We refer the reader to Wakker (2001) and Richter et al. (2001) for discussions of metallicity determination in the IV Arch, which is estimated to be approximately solar.

When examining these results in the context of the galactic fountain, it is important to note that our velocity measurements reflect only local conditions and may not be representative of fountain gas in a global sense. Although the vertical gas velocities we measure are constraining in their own right, our sight lines do not capture gas flows in the transverse direction, which are also critical for understanding fountain kinematics. However, our well-sampled kinematic measurements reinforce and confirm the observed properties of IV HI clouds, which have been successfully reproduced by galactic fountain models (Marasco & Fraternali 2011; Marasco et al. 2012). The dynamics of halo gas in the Milky Way are complex, and these scenarios are highly simplified pictures that we have discussed in isolation. In reality, gas kinematics are driven by an interrelated combination of several mechanisms that continuously supply the disk with gas.

6. Summary

In this work we have performed an analysis of cool ($T \sim 10^4$ K) gas at the Milky Way’s disk–halo interface by examining absorption features of IV ($25 < |v| < 75$ km s $^{-1}$) Ca II and Na I along sight lines to 54 high-latitude BHBs at heights of 3.1–13.4 kpc above the disk in the northern Galactic hemisphere. Distance measurements and dense sight-line sampling allow us to obtain a 3D picture of the spatial extent of the gas, which we

combine with the excellent resolution of Keck HIRES spectra and compare to HI 21 cm emission maps to constrain the characteristics of CGM gas flows.

1. Ca II, and to a lesser extent the more sparsely detected Na I, is spatially coincident with HI emission. The detections are grouped together in the direction away from Galactic center at the edge of two large HI complexes known as the IV Arch and the IV Spur. However, Ca II and HI column densities are not significantly correlated, which may be an observational effect of the large beam size of the EBHIS HI survey, or an indication that HI is associated with gas in a more highly ionized phase (Sections 4.1 and 5; Figures 8 and 10).
2. We find no relationship between column density along a sight line and distance to the background source, indicating that these gas clouds lie close to the disk at $z \lesssim 3.1$ kpc (Section 4.1; Figure 9).
3. We detect virtually no outflowing gas, as well as inflows at velocities of -75 km s $^{-1} < v_z < -25$ km s $^{-1}$. The gas exhibits a clear velocity gradient of ~ 6 – 9 km s $^{-1}$ kpc $^{-1}$ across the disk, which does not correlate with the column density of the gas (Section 4.2; Figures 11 and 13).
4. An analysis of statistical variations in column density suggests that substructure of low ions within warm clouds exists on scales < 500 pc. Most current hydrodynamical simulations do not resolve cool CGM gas on these scales, and greater resolution may be crucial for improving simulations’ chronically low predictions for observed low-ion column densities (Section 4.3; Figure 15).
5. We calculate covering fractions of $f_{\text{Ca II}} = 63^{+6.5}_{-14.0}$ %, $f_{\text{Na I}} = 26^{+5.9}_{-7.6}$ %, and $f_{\text{HI}} = 52\% \pm 5.8\%$ and volume filling factors of $F_{\text{Ca II}} \leq 0.86^{+0.07}_{-0.15}$ %, $F_{\text{Na I}} \leq 0.35^{+0.06}_{-0.08}$ %, and $F_{\text{HI}} \leq 0.63\% \pm 0.06\%$. A comparison of covering fractions for different ions supports a multiphase picture in which small clumps or droplets of cool gas are suspended within larger clouds or streams of hotter, more diffuse gas (Section 4.3.1).

Support for this work was provided by NASA through program GO-14140. J.K.W. acknowledges support from a 2018 Sloan Foundation Fellowship and from the Research Royalty Fund Grant 65-5743 at the University of Washington. A.D. is supported by a Royal Society University Research Fellowship. The optical data presented herein were obtained at the W. M. Keck Observatory, which is operated as a scientific partnership among the California Institute of Technology, the University of California, and the National Aeronautics and Space Administration. The Observatory was made possible by the generous financial support of the W. M. Keck Foundation. The authors wish to recognize and acknowledge the very significant cultural role and reverence that the summit of Maunakea has always had within the indigenous Hawaiian community. We are most fortunate to have the opportunity to conduct observations from this mountain. We thank Chris Howk, Mary Putman, Josh Peek, Karin Sandstrom, Cameron Hummels, Joe Hennawi, and Drummond Fielding for helpful input and discussions about the project. H.V.B. thanks the anonymous referee for numerous suggestions that improved this work. We would also like to acknowledge the participants of the 2018 Arthur M. Wolfe Symposium in Astrophysics and

their role in the exchange of ideas that made this work possible. Finally, A.D. and J.K.W. thank Risa Wechsler and Charlie Conroy for organizing a speed collaboration session at the Mayacamas Ranch Conference in 2015, where the idea for this project originally took shape.

Facility: Keck: HIRES.

Appendix A Milky Way ISM Component Results

A.1. Column Density

ISM component column densities are shown in Figure 16, which can be compared directly with the IV component in Figure 8. Higher Ca II and Na I column density detections are grouped together at positive y values (the direction of Galactic rotation), in contrast to the IV component, which has high Ca II and Na I column density detections clustered together at

positive x values (the direction away from Galactic center). The pattern for HI column densities, which are higher at $x < 8$ kpc, does not match Ca II and Na I for ISM gas as it does for IV gas. The Sun, at $x = 8$ kpc, is nestled just outside the Sagittarius spiral arm of the Milky Way, and the elevated HI column density measurements we measure in that direction can be explained by this feature (Vallée 2016, 2017).

A.2. Kinematics

Figure 17 shows the ISM gas component, which again is directly comparable to the IV component results shown in Figure 11. Detections of Milky Way disk gas (Figure 17) are relatively uniform and show no clear spatial trends in velocity, although most of the gas is moving at negative velocities in the same direction as accreting gas in the IV component. This is somewhat unexpected for normal gas in the disk, which should have an average z -component velocity close to zero relative to

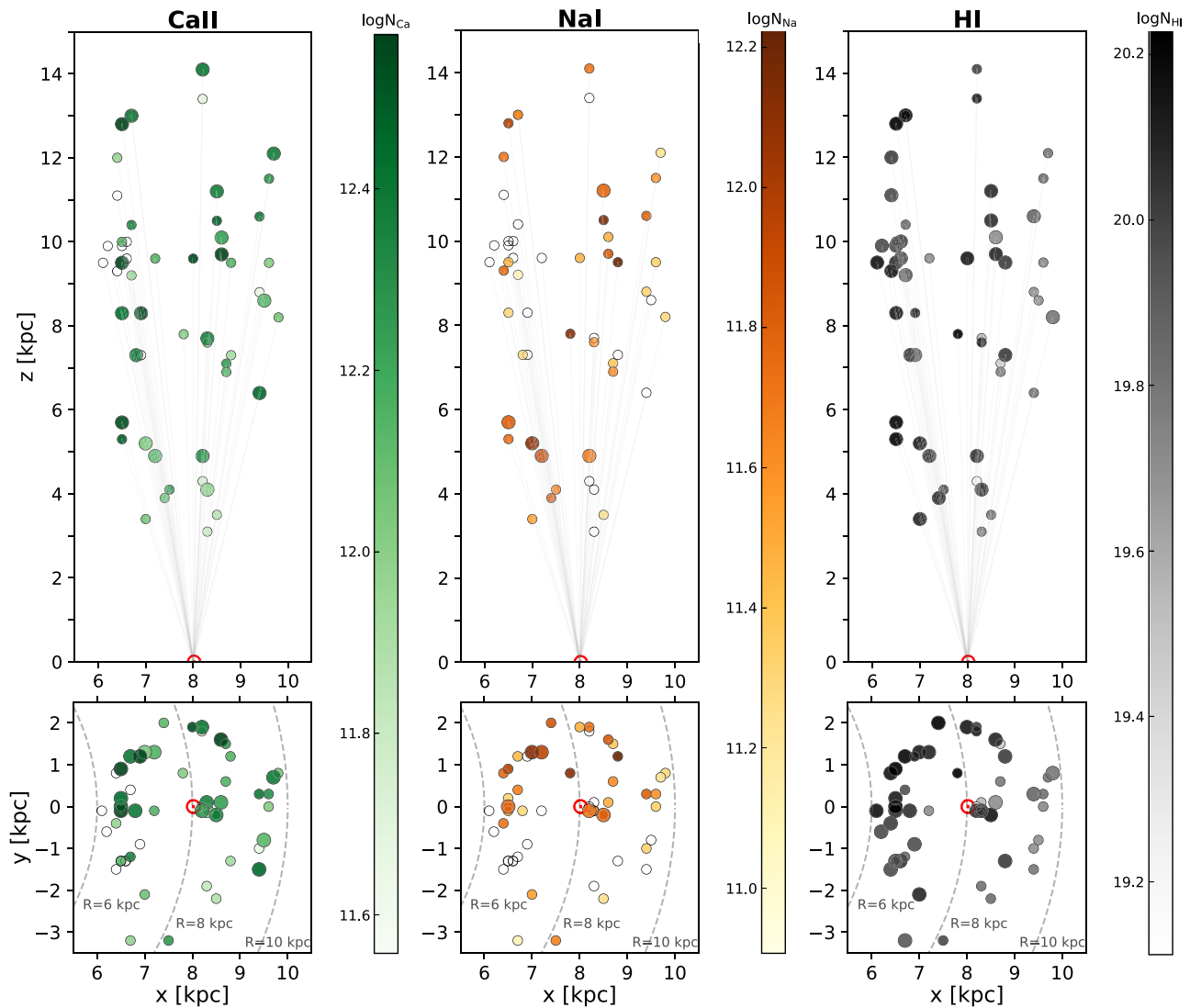


Figure 16. ISM COMPONENT COLUMN DENSITY MEASUREMENTS. Column densities for the ISM component (Milky Way ISM gas, $|v| < 25 \text{ km s}^{-1}$). Markers correspond to background BHB sight lines projected onto the x - y plane of the Milky Way disk. The coordinates for each BHB are plotted in physical kpc units in the plane of the Milky Way; thus, any inferred distance to gas absorption along a sight line is an upper limit. Color indicates column density measurements for Ca II and Na I in absorption and H I in 21 cm emission. Larger markers indicate sight lines along which more than one component was detected, and their colors represent the mean column density of those components. Open circles denote nondetections. The Sun is marked by a red solar symbol, and black dashes denote lines of constant radius from Galactic center.

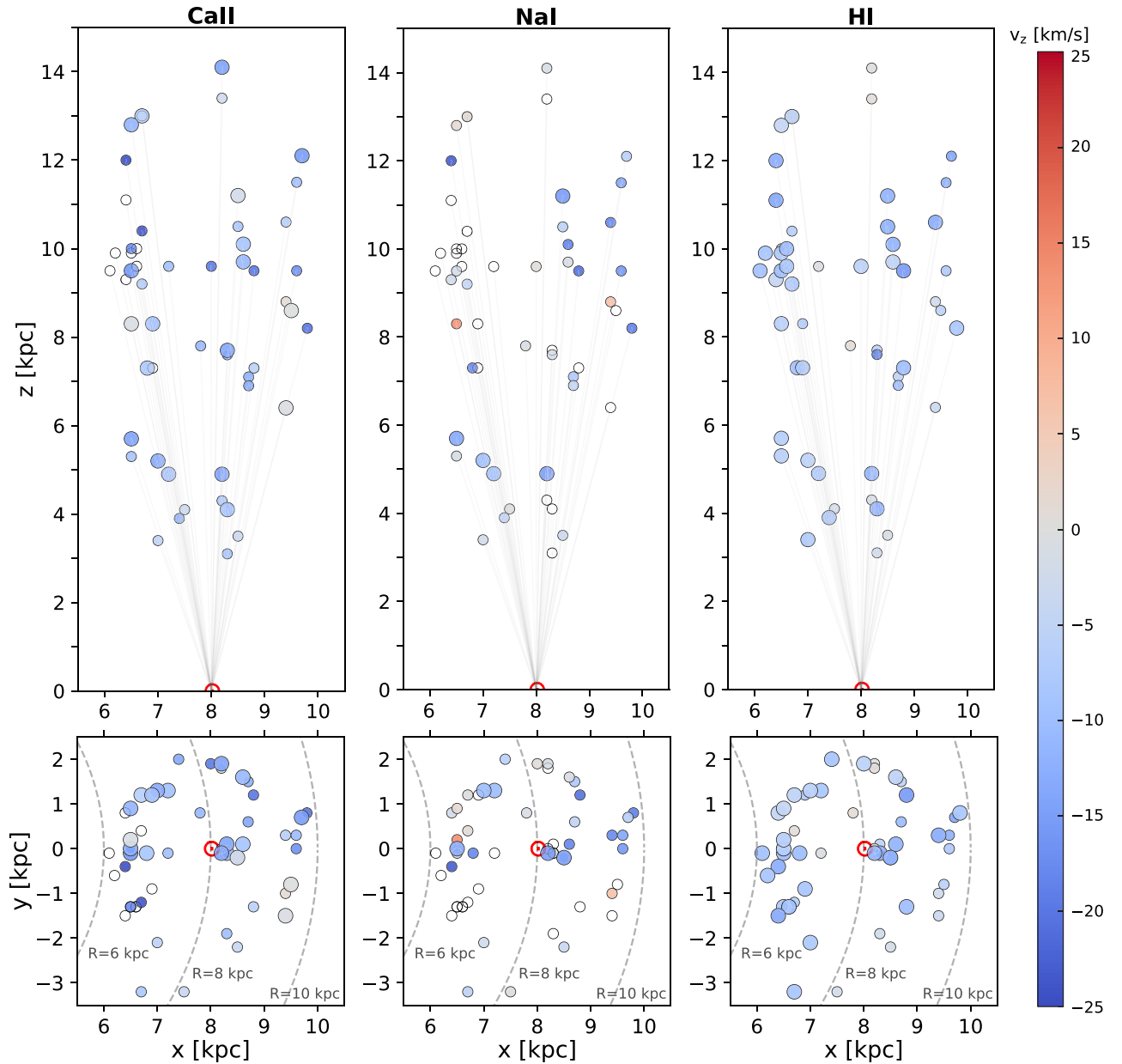


Figure 17. ISM COMPONENT VELOCITY MEASUREMENTS. Velocities for the ISM component (Milky Way ISM gas, $|v| < 25 \text{ km s}^{-1}$). Markers correspond to background BHB sight lines projected onto the x - y plane of the Milky Way disk; thus, any inferred distance to gas absorption along a sight line is an upper limit. Color indicates the component of radial velocity measurements perpendicular to the disk ($v_{\text{LSR}} \sin b$) for Ca II and Na I in absorption and H I in 21 cm emission. Larger markers indicate sight lines along which more than one component was detected, and their colors represent the mean velocity of those components weighted by column density. Open circles denote nondetections. The Sun is marked by a red solar symbol, and black dashes denote lines of constant radius from Galactic center. In contrast to the “IV” component, the Ca II and Na I ISM component does not exhibit any spatial velocity gradient across space.

the LSR. Therefore, it is possible that these metals are not associated with normal ISM gas and are either slow-moving extraplanar gas that was not separated from disk gas by our $|v| < 25 \text{ km s}^{-1}$ velocity cut or gas affected by some other phenomenon within the disk (Zheng et al. 2015).

Appendix B Absorption Features and Line Profile Fits

Figures 18(a)–(g) show a detailed view of Ca II K and Na I D2 absorption features and corresponding H I emission for all BHB sightlines used in this work

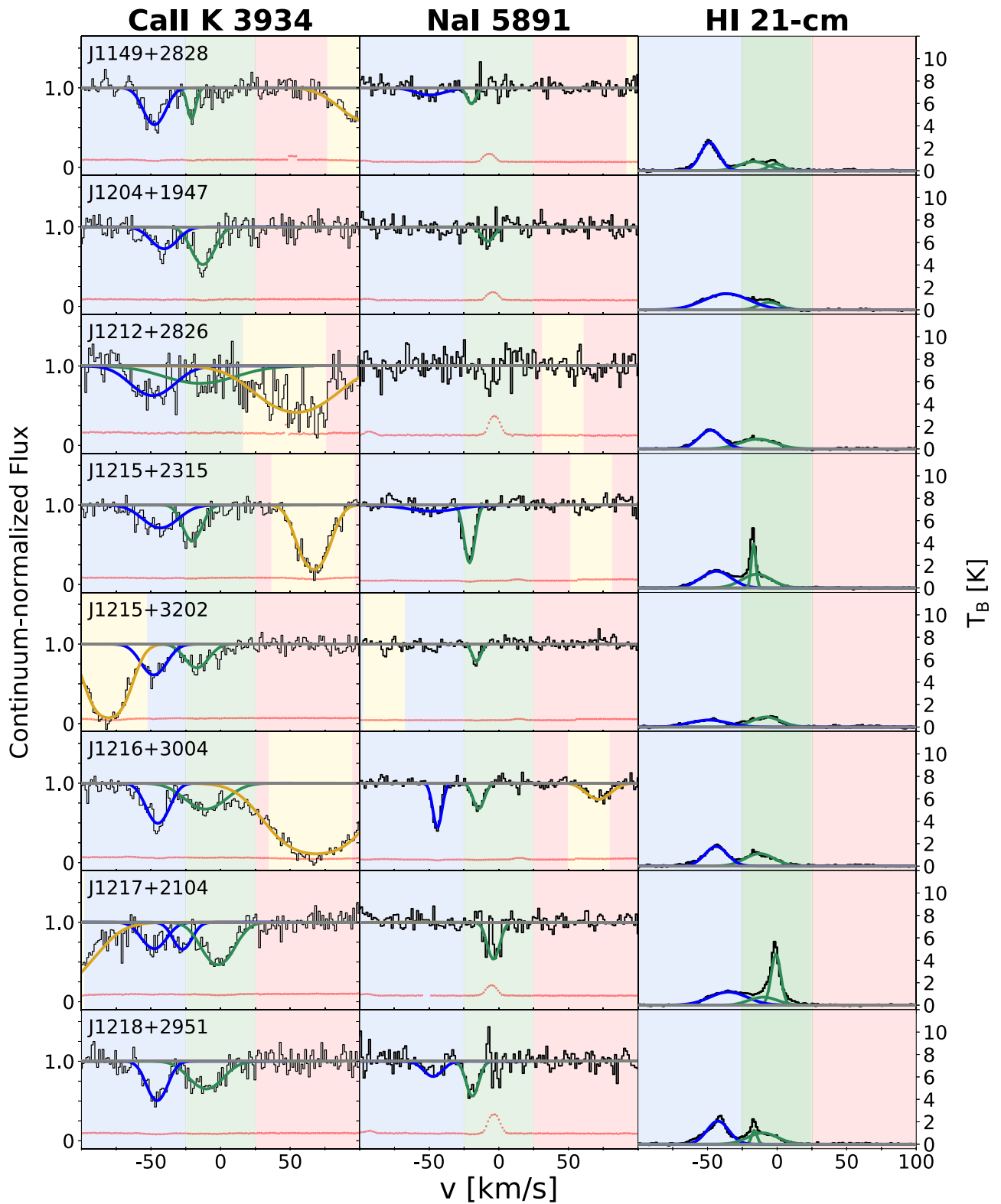


Figure 18. DETAILED VIEW OF ABSORPTION FEATURES. Ca II and Na I absorption features and line profile fits for all BHB sight lines (columns 1 and 2), and H I 21 cm brightness temperatures measured nearest those sight lines (column 3). Flux measurement errors for Ca II and Na I are shown in red. The velocity range and absorption features associated with ISM gas ($|v| < 1$) are shaded green; otherwise, positive velocities are shaded red and negative velocities are shaded blue. Regions near the stellar radial velocity and any associated absorption are highlighted in yellow if they fall within the window of the plot. While the spectra show stellar Ca II absorption in some cases, they rarely show stellar Na I absorption. Almost all absorption detected outside the ISM velocity range is blueshifted, indicating a gaseous component moving toward the disk at approximately -75 to -25 km s^{-1} .

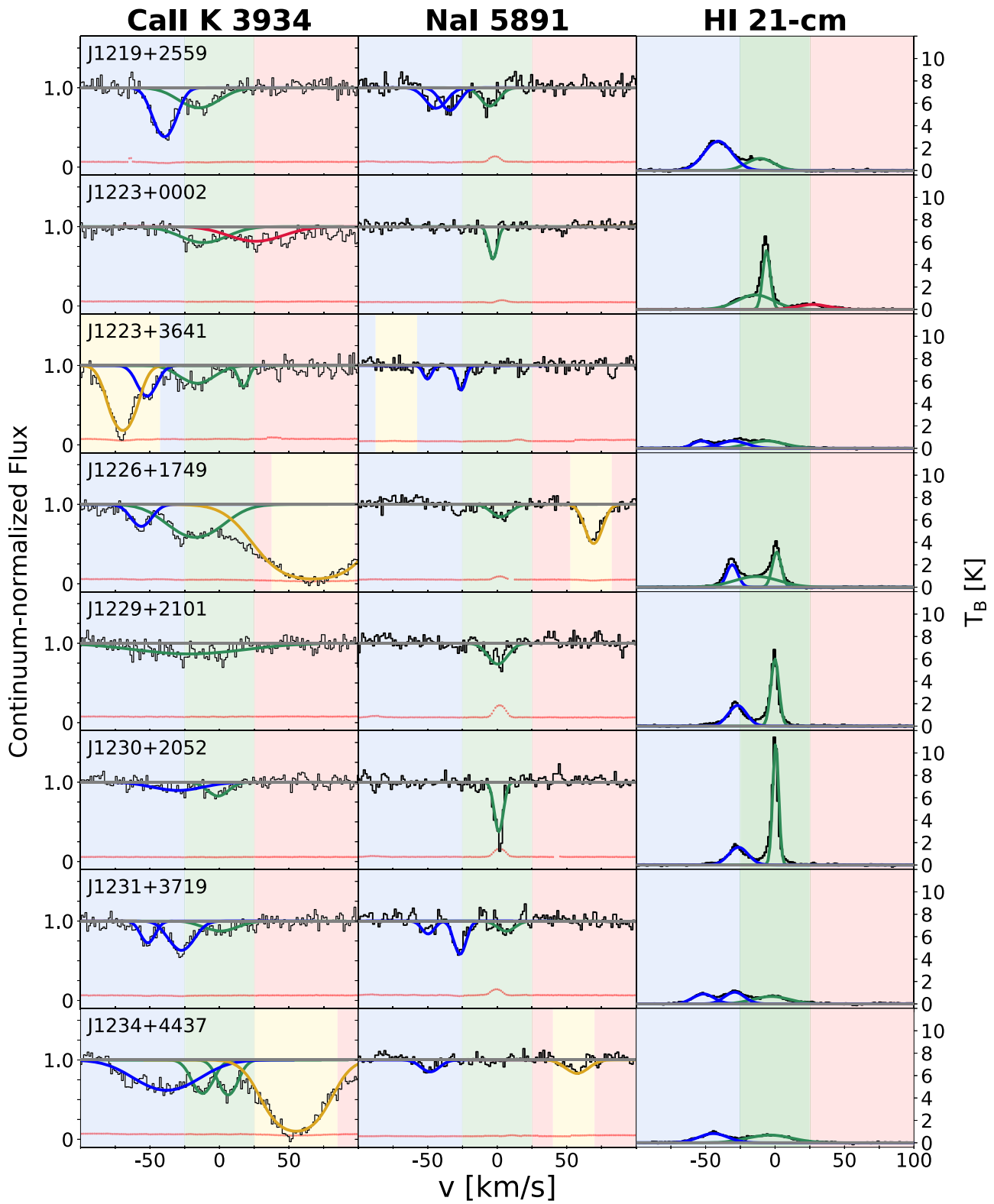


Figure 18. (Continued.)

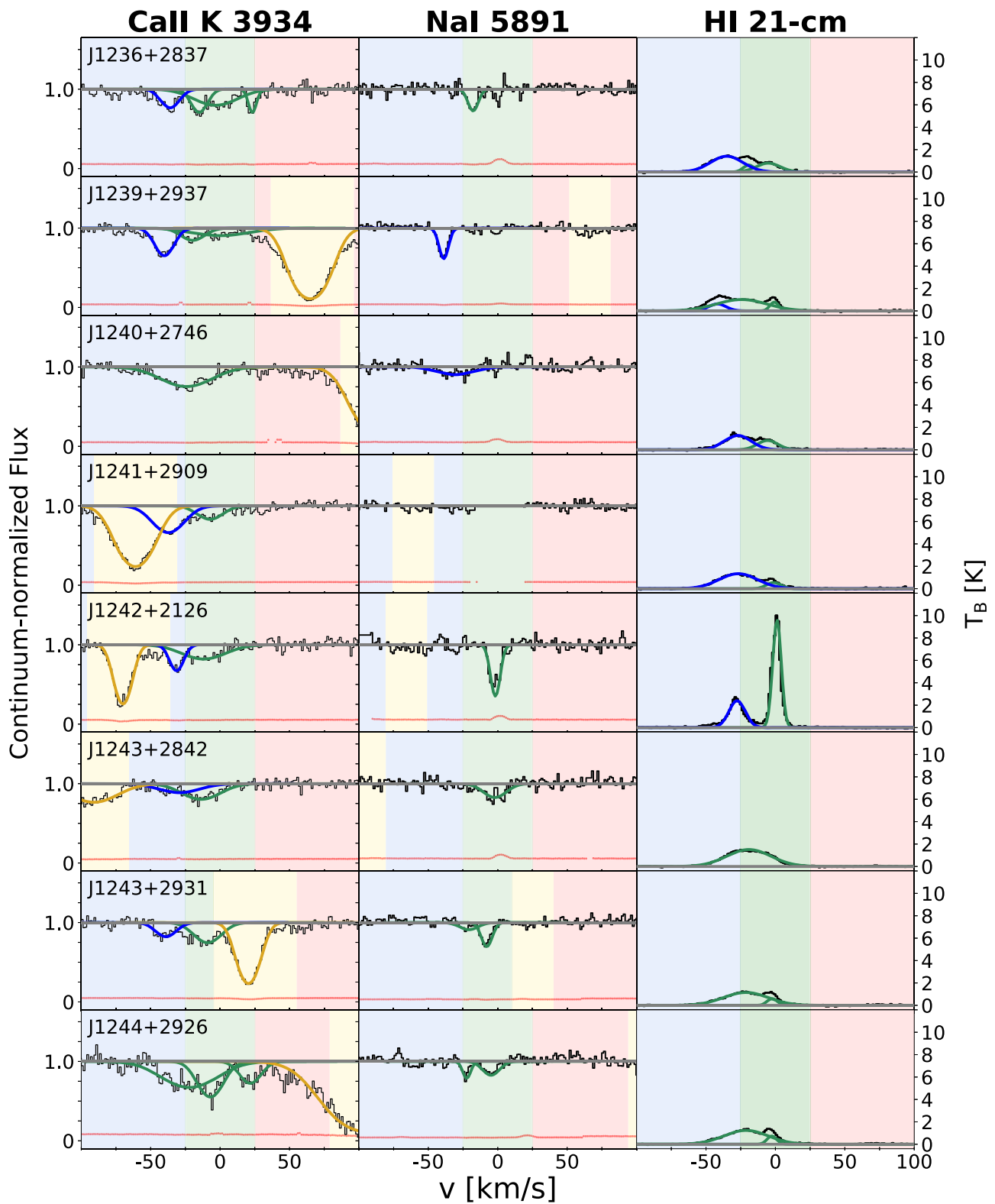


Figure 18. (Continued.)

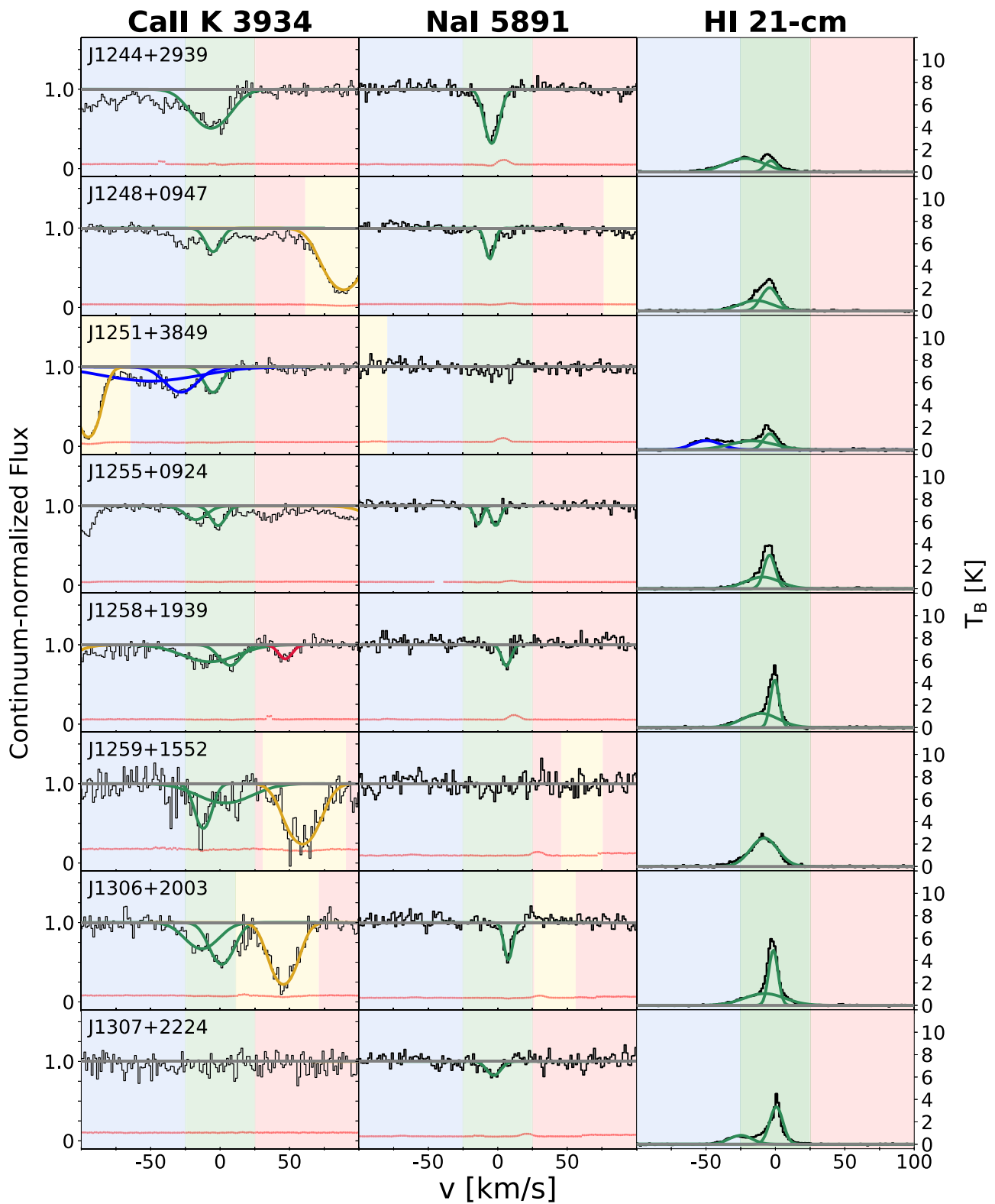


Figure 18. (Continued.)

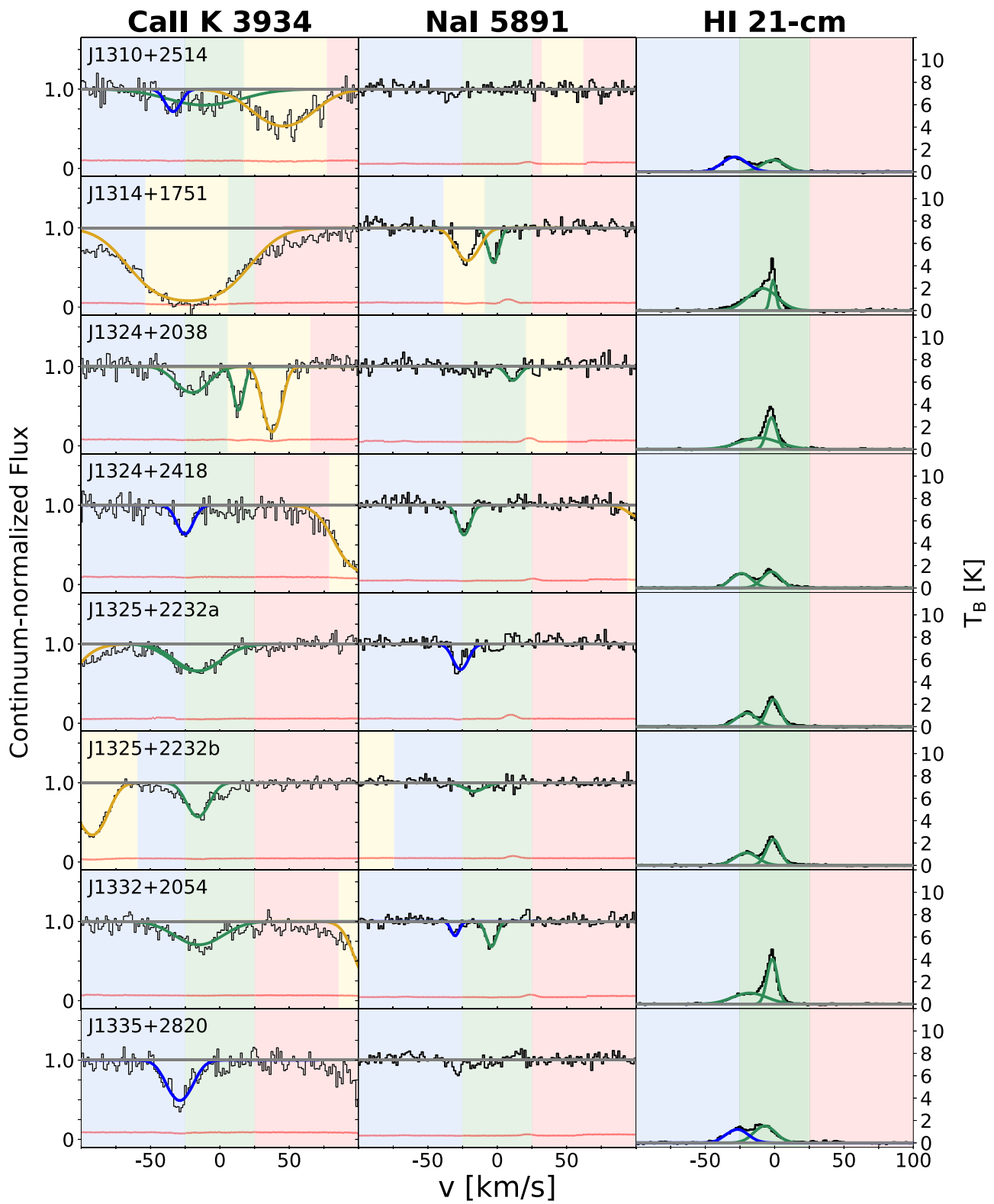


Figure 18. (Continued.)

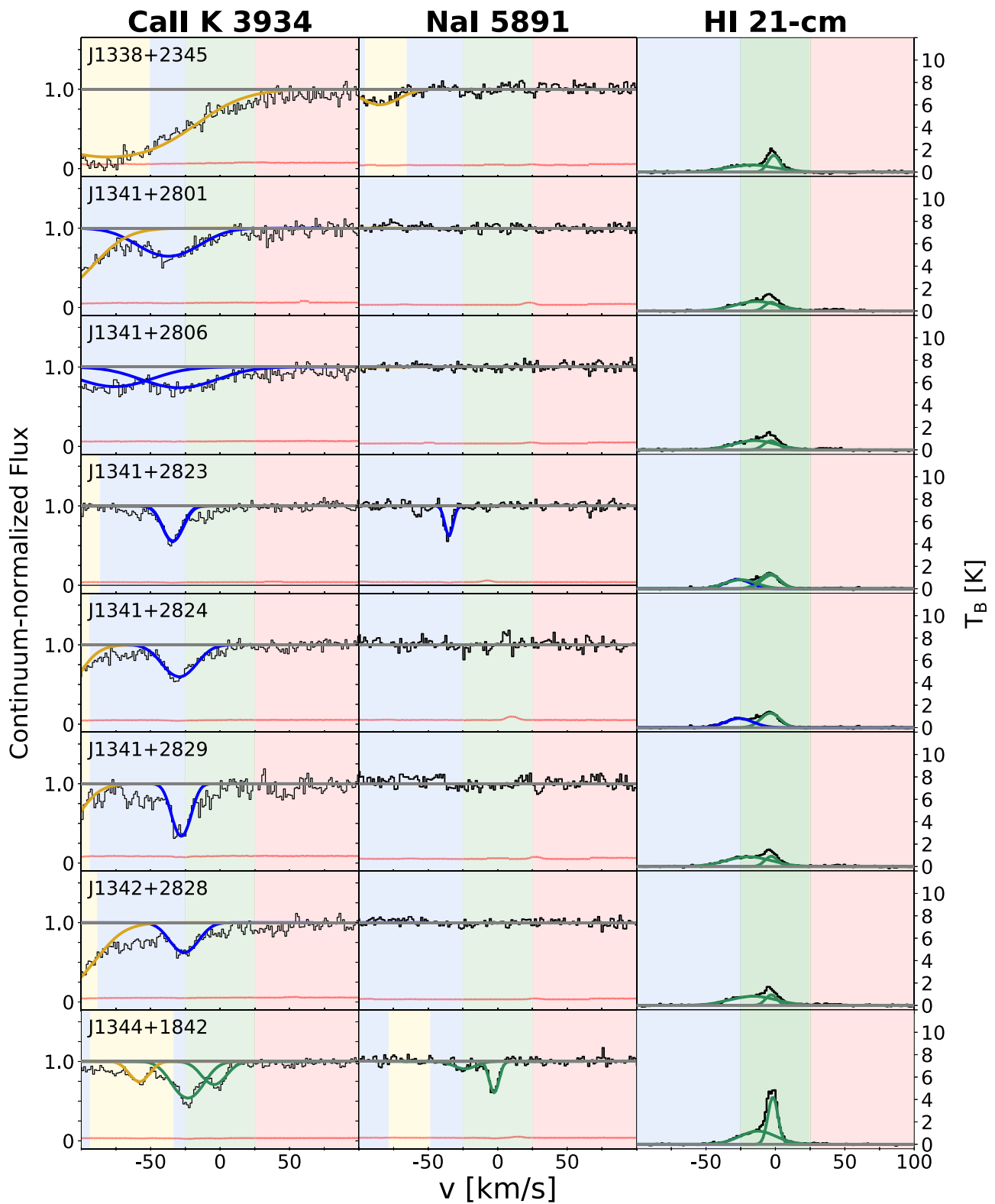


Figure 18. (Continued.)

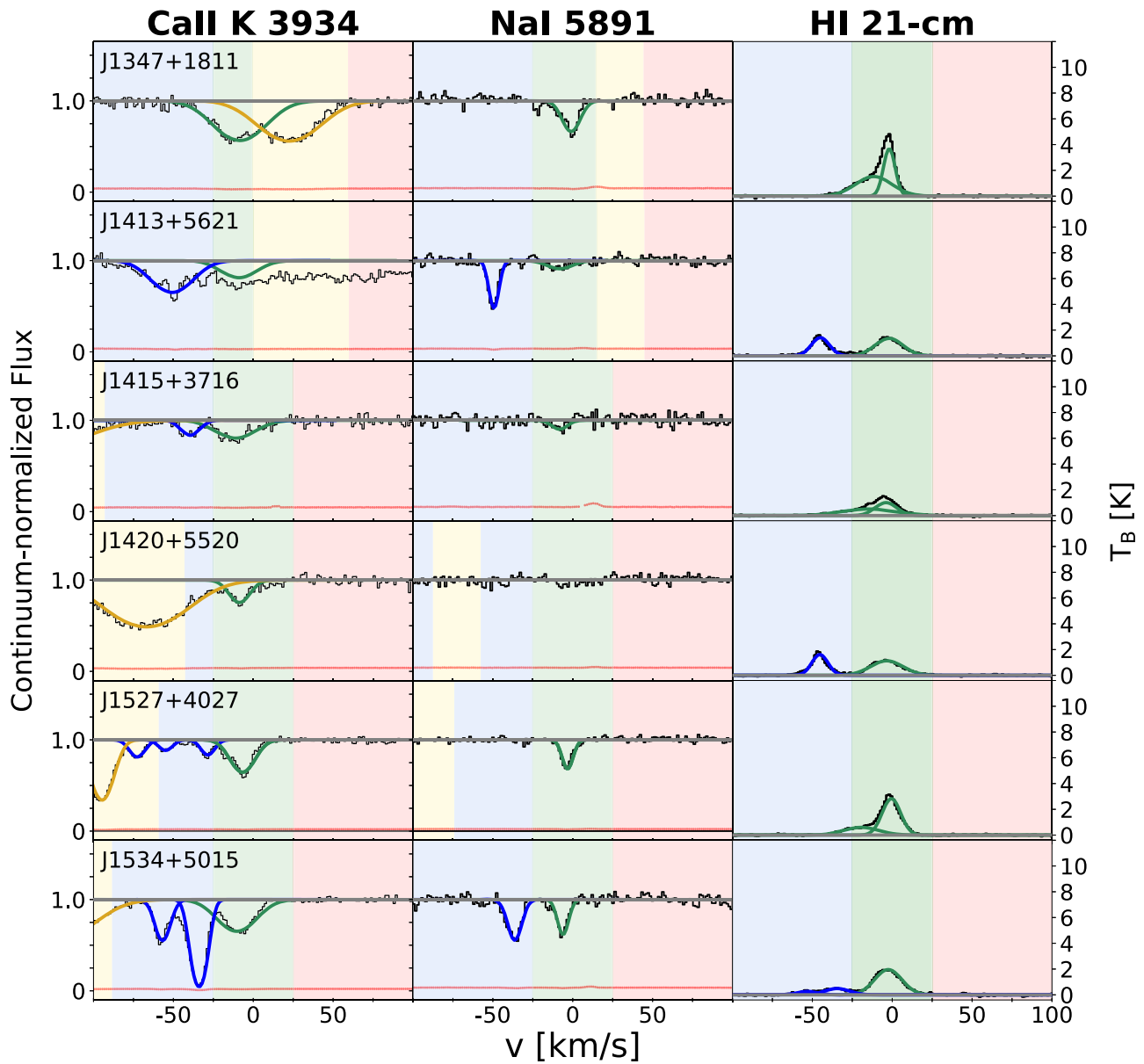


Figure 18. (Continued.)

ORCID iDs

Hannah V. Bish <https://orcid.org/0000-0002-7483-8688>
 Jessica K. Werk <https://orcid.org/0000-0002-0355-0134>
 J. Xavier Prochaska <https://orcid.org/0000-0002-7738-6875>
 Kate H. R. Rubin <https://orcid.org/0000-0001-6248-1864>
 Yong Zheng <https://orcid.org/0000-0003-4158-5116>
 John M. O'Meara <https://orcid.org/0000-0002-7893-1054>
 Alis J. Deason <https://orcid.org/0000-0001-6146-2645>

References

- Albert, C. E., & Danly, L. 2004, *Ap&SS*, 312, 73
 Bahcall, J. N., & Spitzer, L., Jr. 1969, *ApJL*, 156, L63
 Ben Bekhti, N., Richter, P., & Westmeier, T. 2007, *ASSP*, 5, 273
 Bergeron, J. 1986, *A&A*, 155, L8
 Binney, J., Nipoti, C., & Fraternali, F. 2009, *MNRAS*, 397, 1804
 Boettcher, E., Gallagher, J. S., III, & Zweibel, E. G. 2017, *ApJ*, 845, 155
 Bordoloi, R., Fox, A., Lockman, F., et al. 2017, *ApJ*, 834, 191
 Bordoloi, R., Lilly, S., Hardmeier, E., et al. 2014a, *ApJ*, 794, 130
 Bordoloi, R., Lilly, S. J., Kacprzak, G. G., & Churchill, C. W. 2014b, *ApJ*, 784, 108
 Bregman, J. N. 1980, *ApJ*, 236, 577
 Brooks, A. M., Governato, F., Quinn, T., Brook, C. B., & Wadsley, J. 2009, *ApJ*, 694, 396
 Chen, Y.-M., Tremonti, C. A., Heckman, T. M., et al. 2010, *AJ*, 140, 445
 Clewley, L., & Jarvis, M. J. 2006, *MNRAS*, 368, 310
 Collins, J., Shull, J., & Giroux, M. 2009, *ApJ*, 705, 962
 Crighton, N. H. M., Hennawi, J. F., Simcoe, R. A., et al. 2015, *MNRAS*, 446, 18
 de Avillez, M. A. 2000, *Ap&SS*, 272, 23
 Deason, A. J., Belokurov, V., & Evans, N. W. 2011, *MNRAS*, 416, 2903
 Emerick, A., Bryan, G. L., Mac Low, M.-M., et al. 2018, *ApJ*, 869, 94
 Fielding, D., Quataert, E., McCourt, M., & Thompson, T. A. 2017, *MNRAS*, 466, 3810
 Forbes, J. C., & Lin, D. N. C. 2018, arXiv:1810.12925
 Ford, H. A., Lockman, F. J., & McClure-Griffiths, N. M. 2010, *ApJ*, 722, 367
 Foreman-Mackey, D., Hogg, D. W., Lang, D., & Goodman, J. 2013, *PASP*, 125, 306
 Fox, A. J., Bordoloi, R., Savage, B., et al. 2015, *ApJL*, 799, L7
 Fox, A. J., Wakker, B., Barger, K., et al. 2014, *ApJ*, 787, 147
 Fraternali, F. 2017, *Gas Accretion onto Galaxies* (Berlin: Springer), 323

- Fraternali, F., & Binney, J. J. 2006, *MNRAS*, **366**, 449
- Fraternali, F., van Moorsel, G., Sancisi, R., & Oosterloo, T. 2002, *AJ*, **123**, 3124
- Fukui, Y., Hayakawa, T., Inoue, T., et al. 2018, *ApJ*, **860**, 33
- Heald, G., Józsa, G., Serra, P., et al. 2011, *A&A*, **526**, A118
- Heckman, T. M., Alexandroff, R. M., Borthakur, S., Overzier, R., & Leitherer, C. 2015, *ApJ*, **809**, 147
- Heckman, T. M., Lehnert, M. D., Strickland, D. K., & Armus, L. 2000, *ApJS*, **129**, 493
- Howk, J. C., Rueff, K. M., Lehner, N., et al. 2018, *ApJ*, **856**, 166
- Hsu, W. H., Putman, M. E., Heitsch, F., et al. 2011, *AJ*, **141**, 57
- Hummels, C. B., Smith, B., Hopkins, P., et al. 2018, arXiv:1811.12410
- Kalberla, P. M. W., Burton, W. B., Hartmann, D., et al. 2005, *A&A*, **440**, 775
- Karim, M., Fox, A., Jenkins, E., et al. 2018, *ApJ*, **860**, 98
- Kim, C.-G., & Ostriker, E. C. 2018, *ApJ*, **853**, 173
- Kinman, T. D., Suntzeff, N. B., & Kraft, R. P. 1994, *AJ*, **108**, 1722
- Kirby, E. N. 2011, in EAS Publications Ser. 48, The Elemental Abundance Distributions of Milky Way Satellite Galaxies, A Universe of Dwarf Galaxies, ed. M. Koleva, P. Prugniel, & I. Vauglin (Paris: EDP Sciences), 19
- Krumholz, M. R., & Ting, Y.-S. 2018, *MNRAS*, **475**, 2236
- Kuntz, K. D., & Danly, L. 1993, in Star Formation, Galaxies and the Interstellar Medium, ed. J. Franco, F. Ferrini, & G. Tenorio-Tagle (Cambridge: Cambridge Univ. Press), 99
- Kuntz, K. D., & Danly, S. 1996, *ApJ*, **457**, 703
- Lancaster, L., Kuposov, S. E., Belokurov, V., Evans, N. W., & Deason, A. J. 2018, arXiv:1807.04290
- Lehner, N., & Howk, J. C. 2011, *Sci*, **334**, 955
- Liang, C. J., & Remming, I. S. 2018, arXiv:1806.10688
- Luri, X., Brown, A., Sarro, L., et al. 2018, *A&A*, **616**, A9
- Maio, U., Dolag, K., Ciardi, B., & Tornatore, L. 2007, *MNRAS*, **379**, 963
- Maller, A. H., & Bullock, J. S. 2004, *MNRAS*, **355**, 694
- Marasco, A., & Fraternali, F. 2011, *A&A*, **525**, A134
- Marasco, A., Fraternali, F., & Binney, J. J. 2012, *MNRAS*, **419**, 1107
- Marinacci, F., Binney, J., Fraternali, F., et al. 2010, *MNRAS*, **404**, 1464
- Marinacci, F., Fraternali, F., Binney, J., et al. 2012, *European Physical Journal Web of Conferences*, **19**, 08008
- Martin, C. L. 2005, *ApJ*, **621**, 227
- McCourt, M., Oh, S. P., O'Leary, R., & Madigan, A.-M. 2018, *MNRAS*, **473**, 5407
- Millman, K. J., & Aivazis, M. 2011, *CSE*, **13**, 9
- Münch, G., & Zirin, H. 1961, *ApJ*, **133**, 11
- Murga, M., Zhu, G., Ménard, B., & Lan, T.-W. 2015, *MNRAS*, **452**, 511
- Murphy, E., Lockman, F., & Savage, B. 1995, *ApJ*, **447**, 642
- O'Meara, J. M., Lehner, N., Howk, J., et al. 2015, *AJ*, **150**, 111
- Oppenheimer, B. D., Segers, M., Schaye, J., Richings, A. J., & Crain, R. A. 2018, *MNRAS*, **474**, 4740
- Osterman, S., Green, J., Froning, C., et al. 2009, APS Meeting Abstracts, C8.002
- Peeples, M. S., Corlies, L., Tumlinson, J., et al. 2019, *ApJ*, **873**, 129
- Prochaska, J. X., Werk, J. K., Worseck, G., et al. 2017, *ApJ*, **837**, 169
- Puspitarini, L., & Lallement, R. 2012, *A&A*, **545**, A21
- Putman, M., Peek, J., & Joung, M. 2012, *ARA&A*, **50**, 491
- Putman, M. E., de Heij, V., Staveley-Smith, L., et al. 2002, *AJ*, **123**, 873
- Richter, P. 2017, in Gas Accretion onto Galaxies, ed. A. Fox & R. Davé (Berlin: Springer), 15
- Richter, P., Sembach, K. R., Wakker, B. P., et al. 2001, *ApJ*, **559**, 318
- Rubin, K. H. R., Diamond-Stanic, A. M., Coil, A. L., Crighton, N. H. M., & Stewart, K. R. 2018a, *ApJ*, **868**, 142
- Rubin, K. H. R., O'Meara, J., Cooksey, K., et al. 2018b, *ApJ*, **859**, 146
- Rubin, K. H. R., Prochaska, J. X., Koo, D. C., et al. 2014, *ApJ*, **794**, 156
- Rubin, K. H. R., Prochaska, J. X., Koo, D. C., & Phillips, A. C. 2012, *ApJL*, **747**, L26
- Rupke, D. S., Veilleux, S., & Sanders, D. B. 2005, *ApJS*, **160**, 115
- Sancisi, R., Fraternali, F., Oosterloo, T., & van der Hulst, T. 2008, *A&ARv*, **15**, 189
- Savage, B. D., & Sembach, K. R. 1994, *ApJ*, **434**, 145
- Savage, B. D., & Wakker, B. P. 2009, *ApJ*, **702**, 1472
- Schneider, E. E., Robertson, B. E., & Thompson, T. A. 2018, *ApJ*, **862**, 56
- Sembach, K. R., Wakker, B., Savage, B., et al. 2003, *ApJS*, **146**, 165
- Shapiro, P. R., & Field, G. B. 1976, *ApJ*, **205**, 762
- Shull, J., Jones, J., Danforth, C., & Collins, J. 2009, *ApJ*, **699**, 754
- Sirko, E., Goodman, J., Knapp, G., et al. 2004, *AJ*, **127**, 899
- Smoker, J. V., Fox, A. J., & Keenan, F. P. 2011, *MNRAS*, **415**, 1105
- Sparre, M., Pfrommer, C., & Vogelsberger, M. 2019, *MNRAS*, **482**, 5401
- Spitzer, L. J. 1956, *ApJ*, **124**, 20
- Stanimirović, S., Hoffman, S., Heiles, C., et al. 2008, *ApJ*, **680**, 276
- Stern, J., Hennawi, J. F., Prochaska, J. X., & Werk, J. K. 2016, *ApJ*, **830**, 87
- Stocke, J. T., Keeney, B. A., Danforth, C. W., et al. 2013, *ApJ*, **763**, 148
- Su, M., Slatyer, T. R., & Finkbeiner, D. P. 2010, *ApJ*, **724**, 1044
- Sutherland, R. S., & Dopita, M. 1993, *ApJS*, **88**, 253
- Tumlinson, J., Peeples, M. S., & Werk, J. K. 2017, *ARA&A*, **55**, 389
- Vallée, J. P. 2016, *AJ*, **151**, 55
- Vallée, J. P. 2017, *AstRv*, **13**, 113
- van Woerden, H., Wakker, B. P., Schwarz, U. J., & de Boer, K. S. 2005, *Ap&SS*, **312**
- Vogt, S. S., Allen, S. L., Bigelow, B. C., et al. 1994, *Proc. SPIE, Instrumentation in Astronomy VIII*, **2198**, 362
- Wakker, B. P. 2001, *ApJS*, **136**, 463
- Wakker, B. P., & van Woerden, H. 1991, *A&A*, **250**, 509
- Werk, J. K., Prochaska, J. X., Thom, C., et al. 2013, *ApJS*, **204**, 17
- Werk, J. K., Prochaska, J. X., Tumlinson, J., et al. 2014, *ApJ*, **792**, 8
- Werk, J. K., Rubin, K. H. R., Bish, H. V., et al. 2019, arXiv:1904.11014
- Winkel, B., Kerp, J., Flöer, L., et al. 2016, *A&A*, **585**, A41
- Xue, X.-X., Rix, H. W., Yanny, B., et al. 2011, *ApJ*, **738**, 79
- Xue, X. X., Rix, H. W., Zhao, G., et al. 2008, *ApJ*, **684**, 1143
- Zheng, Y., Peek, J. E. G., Putman, M. E., & Werk, J. K. 2017, *ApJ*, **871**, 35
- Zheng, Y., Peek, J. E. G., Werk, J. K., & Putman, M. E. 2017, *ApJ*, **834**, 179
- Zheng, Y., Putman, M. E., Peek, J. E. G., & Joung, M. R. 2015, *ApJ*, **807**, 103